

---

# INVERTING SELF-ORGANIZING MAPS: A UNIFIED ACTIVATION-BASED FRAMEWORK

---

**Alessandro Londei**

Sony Computer Science Laboratories - Rome  
 Joint Initiative CREF-SONY, Centro Ricerche Enrico Fermi  
 Via Panisperna 89/A, 00184  
 Rome, Italy  
 alessandro.londei@sony.com

**Matteo Benati**

Department of Computer, Automatic and Management Engineering  
 Sapienza University, Via Ariosto 25  
 Rome, Italy  
 matteo.benati@uniroma1.it

**Denise Lanzieri**

Sony Computer Science Laboratories - Rome  
 Joint Initiative CREF-SONY, Centro Ricerche Enrico Fermi  
 Via Panisperna 89/A, 00184  
 Rome, Italy  
 denise.lanzieri@sony.com

**Vittorio Loreto**

Sony Computer Science Laboratories - Rome  
 Joint Initiative CREF-SONY, Centro Ricerche Enrico Fermi  
 Via Panisperna 89/A, 00184  
 Rome, Italy  
 Physics Department  
 Sapienza University, Piazzale Aldo Moro 1  
 Rome, Italy  
 Complexity Science Hub  
 Josefstadtter Strasse 39, A 1080, Vienna, Austria  
 vittorio.loreto@sony.com

## ABSTRACT

Self-Organizing Maps (SOMs) provide topology-preserving projections of high-dimensional data and have been widely used for visualization, clustering, and vector quantization. In this work, we show that the activation pattern of a SOM - the squared distances to its prototypes - can be *inverted* to recover the exact input under mild geometric conditions. This follows from a classical fact in Euclidean distance geometry: a point in  $D$  dimensions is uniquely determined by its distances to  $D+1$  affinely independent references. We derive the corresponding linear system and characterize the conditions under which the inversion is well-posed. Building upon this mechanism, we introduce the Manifold-Aware Unified SOM Inversion and Control (MUSIC) update rule, which enables controlled, semantically meaningful trajectories in latent space. MUSIC modifies squared distances to selected prototypes while preserving others, resulting in a deterministic geometric flow aligned with the SOM's piecewise-linear structure. Tikhonov regularization stabilizes the update rule and

ensures smooth motion on high-dimensional datasets. Unlike variational or probabilistic generative models, MUSIC does not rely on sampling, latent priors, or encoder–decoder architectures. If no perturbation is applied, inversion recovers the exact input; when a target cluster or prototype is specified, MUSIC produces coherent semantic variations while remaining on the data manifold. This leads to a new perspective on data augmentation and controllable latent exploration based solely on prototype geometry. We validate the approach using synthetic Gaussian mixtures, the MNIST digits dataset, and the “Faces in the Wild” dataset. Across all settings, MUSIC produces smooth, interpretable trajectories that reveal the underlying geometry of the learned manifold, illustrating the advantages of SOM-based inversion over unsupervised clustering or random reference sets.

**Keywords** First keyword · Second keyword · More

## 1 Introduction

Self-Organizing Maps (SOMs) [1, 2] are classical topology–preserving neural models that embed high–dimensional data into a structured two-dimensional lattice of prototype vectors. Through competitive learning and neighbourhood cooperation, a SOM organizes prototypes so that nearby units respond to similar inputs, providing an interpretable low-dimensional representation of the data manifold. This property has made SOMs influential in applications ranging from image analysis [3], remote sensing [4], and speech processing [5], to genomics [6], robotics [7], and exploratory visualization [8]. Over the years, several architectural variants—such as Growing Neural Gas [9], Dynamic SOMs [10], hierarchical maps [11], and prototype–regularized deep models like SOM–VAE [12]—have extended the expressive power of SOM–based learning while preserving its foundation in prototype geometry.

Traditionally, SOMs are used as a form of structured vector quantization: each input  $z \in \mathbb{R}^D$  is associated with its Best–Matching Unit (BMU), and the BMU index serves as a discrete representation of the data. In this work, we adopt a fundamentally different viewpoint. Rather than mapping data *to* prototypes, we show that the SOM activation pattern—specifically, the squared distances from  $z$  to all prototypes—contains enough geometric information to *reconstruct*  $z$  exactly. We show that SOM activations can be deterministically inverted to recover the exact input. A complete derivation and the geometric conditions for invertibility are given in Section 2. This inversion mechanism is fully deterministic, non-probabilistic, and does not rely on any generative decoder or latent prior.

Building on this observation, we introduce a unified geometric framework for continuous semantic transformations on the data manifold. Our method proceeds in three steps:

1. **Exact inversion.** From the squared–distance activations to the prototypes, solve a linear system to recover the input vector  $z$ . When the SOM prototypes span  $\mathbb{R}^D$ , inversion is exact up to machine precision.
2. **Structured perturbation of activations.** We selectively modify the squared distances to a chosen subset of prototypes (e.g., a target cluster or a single prototype) while preserving the others. These perturbations must satisfy Euclidean realizability constraints, which we enforce via a Tikhonov–regularized linear system.
3. **MUSIC update rule.** The resulting *Manifold–Aware Unified SOM Inversion and Control* (MUSIC) update produces a latent step  $\Delta z$  that simultaneously moves toward the desired prototypes while maintaining consistency with the preserved distances.

This framework turns a SOM from a static discretizer into a continuous, interpretable mechanism for latent–space exploration. Unlike generative models such as VAEs [13], VQ–VAEs [14], or diffusion models [15], MUSIC does not sample from a learned decoder nor interpolate through a neural architectural latent space. Its behaviour is governed entirely by prototype geometry. If no conditioning is applied, inversion reproduces the *exact* input; when conditioning is introduced, MUSIC yields semantically meaningful variations that remain on the manifold encoded by the SOM.

We validate the method across datasets of increasing geometric and semantic complexity: synthetic Gaussian mixtures (where ground truth geometry is known), handwritten digits (MNIST), and natural face images encoded by a pretrained autoencoder. Across all settings, MUSIC generates coherent semantic flows, preserves local identity where appropriate, and enables controlled transformations specified by prototype clusters or user–selected anchors. The contributions of this paper are therefore twofold: (i) showing that classical SOM activations admit exact inversion through distance geometry, and (ii) introducing a principled update rule that turns the SOM into a geometry–aware engine for semantic latent–space interpolation.

## 2 Inverting Self-Organizing Maps

A Self-Organizing Map (SOM) can be regarded not only as a topographic quantizer but also as a nonlinear embedding between input and activation spaces. Let  $\{w_j\}_{j=1}^N \subset \mathbb{R}^D$  denote the prototype (weight) vectors of a trained SOM. For any input vector  $z \in \mathbb{R}^D$ , define the *squared distance activation vector*

$$a(z) = \begin{bmatrix} a_1(z) \\ \vdots \\ a_N(z) \end{bmatrix}, \quad a_j(z) = \|z - w_j\|^2.$$

We work with *squared* distances because  $a_j(z)$  has linear first-order variation,  $da_j(z) = 2(z - w_j)^\top dz$ , yielding a well-conditioned local Jacobian. Moreover, subtracting any reference activation  $a_r(z)$  removes the common quadratic term  $\|z\|^2$ , exposing an *affine* dependence on  $z$  that will be crucial for exact inversion. The mapping  $f : \mathbb{R}^D \rightarrow \mathbb{R}^N$ ,  $f(z) = a(z)$ , encodes the geometric relationship between the input and all prototypes and can be interpreted as the activation state of the SOM when exposed to  $z$ . Recovering  $z$  from its distances to a sufficiently rich set of prototypes is a standard consequence of Euclidean distance geometry and multilateration (e.g., [16, 17, 18, 19]).

A key property of  $f$  is its equivariance under rigid motions of the prototype set: for any translation  $t \in \mathbb{R}^D$  and rotation  $R \in O(D)$ ,

$$a_j(Rz + t) = \|Rz + t - (Rw_j + t)\|^2 = \|z - w_j\|^2.$$

Hence, the activations are invariant under joint translations and rotations of  $(z, \{w_j\})$ , and only the *relative* configuration of prototypes matters for inversion.

### 2.1 Exact Inversion Property of the SOM Distance Mapping

The following proposition establishes that  $f$  is injective and exactly invertible under mild rank conditions. This property establishes the mathematical foundation for SOM inversion: once activations uniquely determine their generating input, one can reconstruct or manipulate inputs directly through their activation patterns.

**Proposition 1** (Exact Inversion Property). *If the prototype set  $\{w_j\}_{j=1}^N$  spans  $\mathbb{R}^D$ , i.e.  $\text{rank}([w_1 - w_N, \dots, w_{N-1} - w_N]) = D$ , then the mapping  $f$  is injective. Moreover, the input vector  $z$  can be exactly reconstructed from the activation differences  $\{a_j(z) - a_N(z)\}_{j=1}^{N-1}$  by solving a linear system:*

$$z = (B^\top B)^{-1} B^\top c,$$

where

$$B = \begin{bmatrix} 2(w_N - w_1)^\top \\ \vdots \\ 2(w_N - w_{N-1})^\top \end{bmatrix} \in \mathbb{R}^{(N-1) \times D}, \quad c = \begin{bmatrix} a_1(z) - a_N(z) + \|w_N\|^2 - \|w_1\|^2 \\ \vdots \\ a_{N-1}(z) - a_N(z) + \|w_N\|^2 - \|w_{N-1}\|^2 \end{bmatrix}.$$

*Proof.* By definition, each squared activation can be expanded as

$$a_j(z) = z^\top z - 2z^\top w_j + \|w_j\|^2.$$

Subtracting the expression for  $a_N(z)$  eliminates the quadratic term  $z^\top z$ :

$$a_j(z) - a_N(z) = 2(w_N - w_j)^\top z + \|w_j\|^2 - \|w_N\|^2, \quad j = 1, \dots, N-1.$$

This defines an affine system  $Bz = c$ , where  $B$  and  $c$  are as above. If the matrix  $B$  has full column rank  $D$ , its Moore-Penrose pseudoinverse provides a unique solution

$$z = B^+ c = (B^\top B)^{-1} B^\top c, \tag{1}$$

and the reconstruction is exact up to numerical precision. Therefore,  $f$  is injective and the inverse mapping  $f^{-1}$  is linear in the activation differences.  $\square$

The reference index  $N$  is arbitrary: any anchor  $r \in \{1, \dots, N\}$  yields an equivalent linear system built from the differences  $\{a_j(z) - a_r(z)\}$ . In practice, centering the prototypes (e.g., subtracting their mean) and optionally whitening  $z$  and  $\{w_j\}$  can further improve the conditioning of  $B$  without affecting exactness.

This linearization connects to classical Euclidean distance geometry: activation differences form an affine slice of a Euclidean Distance Matrix (EDM), whose embedding is unique up to rigid motions under mild rank conditions [16, 17, 20].

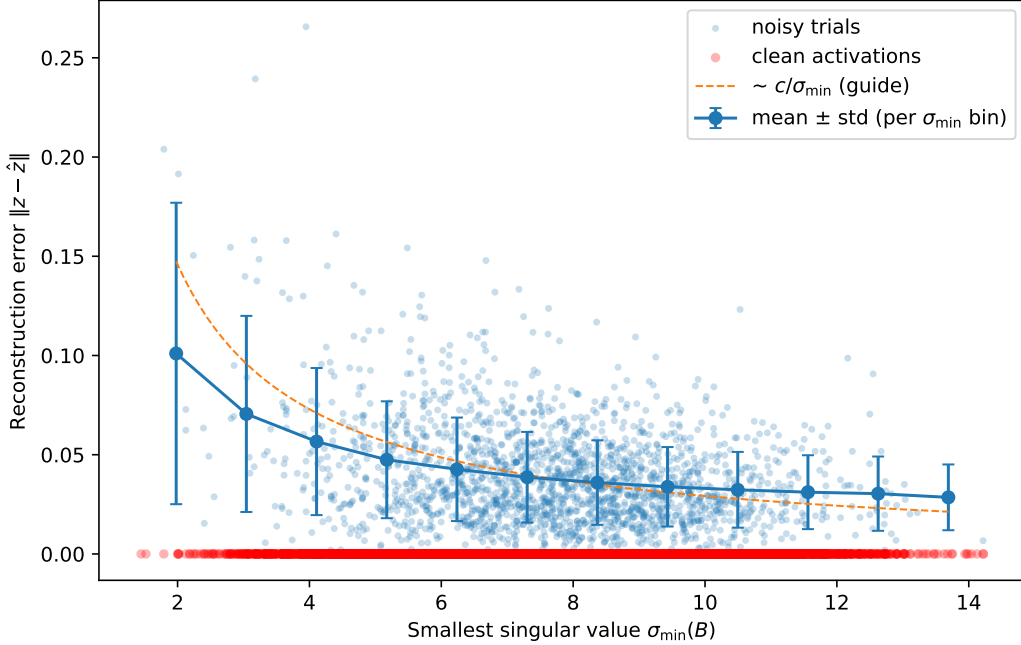


Figure 1: **Inversion accuracy vs. conditioning of the prototype geometry.** For each random prototype set  $W$  and point  $z$ , we form the anchored linear system  $Bz = c$  derived from squared-distance activations. *Clean activations* (red) lead to reconstructions at machine precision across all conditioning levels, demonstrating exact invertibility whenever  $B$  has full column rank. Adding Gaussian noise to activations perturbs the right-hand side of  $Bz = c$  and induces reconstruction errors that grow roughly as  $1/\sigma_{\min}(B)$ . The noisy trials (scatter) and binned mean  $\pm$  std curves (blue circles with error bars) clearly follow this inverse trend: well-spread, affine-independent prototypes yield stable inversion, whereas nearly collinear configurations amplify noise dramatically.

**Corollary 1** (Stability to activation noise). *Let  $\tilde{a}_j(z) = a_j(z) + \varepsilon_j$  with  $\varepsilon \sim \mathcal{N}(0, \sigma^2 I)$ . If  $B$  has full column rank, the least-squares inverse satisfies*

$$\|\hat{z} - z\| \leq \|B^+\| \|\tilde{c} - c\| \leq \|B^+\| \sigma \sqrt{N-1},$$

where  $B^+$  is the Moore–Penrose pseudoinverse. Hence, inversion is Lipschitz–stable, and the amplification factor is governed by the inverse of the smallest singular value of  $B$ ; improving  $B$ ’s conditioning (e.g., via prototype placement or whitening) improves stability.

Figure 1 empirically validates the least-squares stability bound, showing that the reconstruction error  $\|\hat{z} - z\|_2$  increases as the smallest singular value  $\sigma_{\min}(B)$  decreases: across 20,000 noisy trials, binwise means (with standard deviations) follow the predicted inverse trend from

$$\mathbb{E} \|\hat{z} - z\|_2^2 = \sigma^2 \text{tr}((B^\top B)^{-1}) \lesssim \sigma^2 \frac{D}{\sigma_{\min}^2(B)}.$$

If activation noise has covariance  $\Sigma$  (i.e.,  $\varepsilon \sim \mathcal{N}(0, \Sigma)$ ), the optimal inverse is the weighted least-squares solution  $\hat{z} = \arg \min_z \|(Bz - c)\|_{\Sigma^{-1}}^2$ , i.e.,  $\hat{z} = (B^\top \Sigma^{-1} B)^{-1} B^\top \Sigma^{-1} c$ , with stability governed by the smallest eigenvalue of  $B^\top \Sigma^{-1} B$ .

**Lemma 1** (Rank condition and affine independence). *Let  $r$  be any anchor index and  $B_r$  the matrix built from the rows  $2(w_r - w_j)^\top$ ,  $j \neq r$ . Then  $\text{rank}(B_r) = D$  if and only if the set  $\{w_j\}$  contains  $D+1$  affinely independent points. Consequently, the full column rank of  $B_r$  is equivalent to the injectivity of  $f$  from activation differences to inputs.*

Exact inversion requires that the SOM prototypes span the ambient latent space. When the raw input dimension is very large or exceeds the rank of the prototype matrix, dimensionality reduction (e.g., PCA or an autoencoder bottleneck) is necessary. This is a structural property of distance geometry; inversion cannot succeed if the prototypes do not form a basis for the space in which the distance measurements are taken.

The following lemma extends this rank condition to the local differential level, ensuring that the Jacobian of the activation map has full rank everywhere.

**Lemma 2** (Full rank of the activation Jacobian). *Let  $J(z) \in \mathbb{R}^{N \times D}$  be the Jacobian with rows  $J_j(z) = \nabla_z a_j(z)^\top = 2(z - w_j)^\top$ . If the prototypes  $\{w_j\}$  contain  $D+1$  affinely independent points, then  $\text{rank } J(z) = D$  for all  $z \in \mathbb{R}^D$ .*

*Proof.* Fix any anchor  $r$ . Since  $\{w_j - w_r\}_{j \neq r}$  span  $\mathbb{R}^D$ , the set  $\{z - w_j\}_{j \neq r}$  spans the same linear space because  $z - w_j = (z - w_r) - (w_j - w_r)$ . Hence the rows of  $J(z)$  span  $\mathbb{R}^D$ , so  $\text{rank } J(z) = D$ .  $\square$

The proof reveals that the inversion depends only on relative prototype positions and distance differences, independent of the absolute scale of activations. The linear system  $Bz = c$  is the algebraic counterpart of a well-known distance-geometry fact.

For overcomplete maps ( $N > D+1$ ), the system is consistent, and inversion reduces to least squares,  $\hat{z} = B^+c$ , with reconstruction error driven by floating-point precision and the conditioning of  $B$ . In double precision, we typically observe errors on the order of  $10^{-18}$ .

This exact-inversion property establishes the SOM activation map as a mathematically well-posed latent representation. In the next section, we exploit this property to define small, consistent perturbations in activation space that translate into interpretable input variations.

### 3 Perturbing the SOM activation layer

Having established that the distance-based activation map admits exact inversion under mild conditions, we now use it as a control interface for exploration. We perturb distances to selected prototypes – typically anchored around the current BMU and its Voronoi neighborhood – and recover the corresponding latent update by solving a small, regularized inverse problem. The resulting trajectory modifies the activation pattern in a targeted way while remaining geometrically consistent, yielding smooth and semantically meaningful variations of  $z$ .

We denote by  $\text{BMU}(z) = \arg \min_j \|z - w_j\|$  the best-matching unit (prototype with minimal distance) and by  $\mathcal{V}_j$  its Voronoi region [21]. The collection  $\{\mathcal{V}_j\}$  forms a Voronoi tessellation of the input space, providing the piecewise-linear partition underlying the SOM topology. Building upon the exact invertibility of the activation mapping established in the previous section, we reinterpret the SOM activation layer as a geometrically consistent latent manifold for controlled exploration of the input domain. Each input vector  $z \in \mathbb{R}^D$  induces a structured activation pattern  $a(z) = \{\|z - w_j\|^2\}_{j=1}^N$  representing its geometric relationships to all prototypes. Small, geometrically consistent perturbations of this activation pattern yield smooth and semantically coherent variations of  $z$ , provided the modified activations remain compatible with a valid Euclidean configuration. Conceptually, this approach parallels latent-space editing in generative models, where smooth variations in internal representations yield coherent transformations of inputs. Unlike those models, however, the SOM activation manifold is explicitly geometric, making the consistency constraints analytically tractable. In contrast, arbitrary changes of single activations generally violate the Euclidean consistency of the representation, as the distances to all prototypes are mutually dependent ([21], [22], [23]). Figure 2 illustrates this geometric interdependence for a perturbation applied to a single prototype.

To introduce a valid perturbation, we seek the smallest change  $\Delta z \in \mathbb{R}^D$  that produces a prescribed modification in the distance to a selected prototype while approximately preserving the geometry of the other distances. Let

$$z \in \mathbb{R}^D, \quad \{w_j\}_{j=1}^N \subset \mathbb{R}^D, \quad k \in \{1, \dots, N\}, \quad \Delta d_k \in \mathbb{R},$$

where  $w_j$  are the prototype vectors and  $\Delta d_k$  is the desired increment in the distance between  $z$  and  $w_k$ . The goal is to determine a perturbation vector  $\Delta z$  satisfying:

1. the distance to prototype  $k$  changes by  $\Delta d_k$ ;
2. the norm  $\|\Delta z\|$  is minimal (scaled by a user-defined parameter  $r_{\text{scale}}$ );
3. the relative geometry of all other distances is approximately preserved.

We can now derive the analytic form of the minimal perturbation consistent with these constraints. Defining the relative position and current distance

$$x := z - w_k, \quad d_k := \|x\|, \quad d'_k := d_k + \Delta d_k,$$

the desired squared change in distance is

$$\Delta d_k^2 = (d'_k)^2 - d_k^2 = \|x + \Delta z\|^2 - \|x\|^2.$$

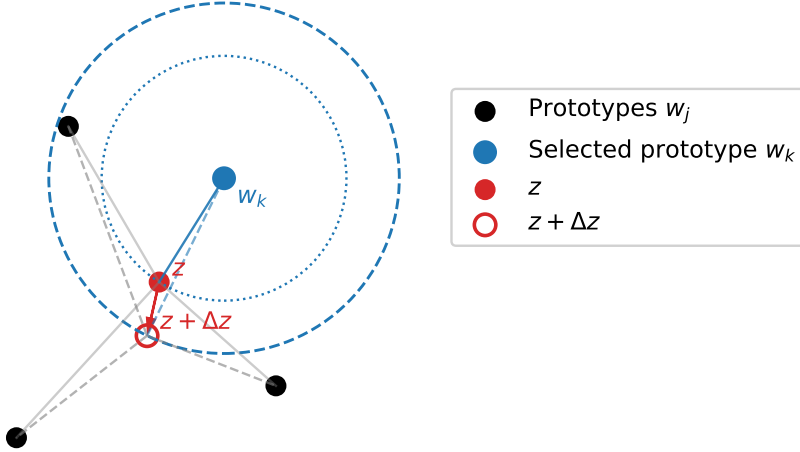


Figure 2: **Geometric schematic of a single-cell perturbation in the SOM activation space.** A small displacement  $\Delta z$  of the input vector  $z$  modifies its distance to the selected prototype  $w_k$ , thereby inducing a consistent reconfiguration of distances to all other prototypes  $w_j$ . Solid lines indicate the original distances  $\|z - w_j\|$ , and dashed lines the updated distances  $\|z + \Delta z - w_j\|$ . Because all distances are mutually constrained by the geometry of  $\mathbb{R}^D$ , a perturbation of one activation cell necessarily entails a coordinated adaptation of the others to maintain a valid Euclidean configuration.

Expanding gives

$$\|x + \Delta z\|^2 = \|x\|^2 + 2x^\top \Delta z + \|\Delta z\|^2,$$

and thus

$$2x^\top \Delta z + \|\Delta z\|^2 = \Delta d_k^2.$$

This identity isolates the radial component of the displacement relative to  $w_k$ .

For infinitesimal perturbations, the quadratic term  $\|\Delta z\|^2$  is second-order and can be neglected relative to the linear term  $2x^\top \Delta z$ , yielding the first-order constraint:

$$x^\top \Delta z = c := \frac{1}{2} \Delta d_k^2.$$

This constraint fixes the projection of  $\Delta z$  along  $x$ . Decomposing the perturbation as

$$\Delta z = \Delta z_{\parallel} + \Delta z_{\perp}, \quad \Delta z_{\parallel} = \frac{c}{\|x\|^2} x, \quad x^\top \Delta z_{\perp} = 0,$$

one obtains a parallel component that achieves the desired change in distance and an orthogonal component spanning the local isodistance subspace. Geometrically,  $\Delta z_{\perp}$  belongs to the local tangent space of the SOM distance manifold: in the idealized linear regime, such directions leave the vector of squared distances approximately unchanged, producing a locally isometric motion of  $z$  up to first order. The radial-tangential decomposition holds in any ambient dimension  $D$ , but increasing  $D$  enlarges the tangential subspace to dimension  $D-1$  and typically strengthens the distance-preservation effect of tangential motion. Indeed, for  $\Delta z_{\perp}$  constrained to be orthogonal to  $x$ , the first-order variation of each squared distance satisfies

$$\Delta a_j \approx 2(z - w_j)^\top \Delta z_{\perp} = 2c_j^\top \Delta z_{\perp}, \quad c_j := w_k - w_j,$$

since  $x^\top \Delta z_{\perp} = 0$ . When the prototype offsets  $\{c_j\}$  are well spread and  $\Delta z_{\perp}$  is not preferentially aligned with any specific  $c_j$ , dot products concentrate in high dimension, yielding the typical scaling

$$|c_j^\top \Delta z_{\perp}| \sim \|\Delta z_{\perp}\| \|c_j\| / \sqrt{D}.$$

Consequently, tangential perturbations become increasingly close to isometries as  $D$  grows (in a typical-case sense), while the  $O(\|\Delta z\|^2)$  remainder of the Taylor expansion still controls the ultimate accuracy of the linear approximation.

A geometric illustration of the radial-tangential decomposition and its effect on all SOM prototypes is provided in Figure 3. For a formal explanation of why tangential directions preserve all Euclidean distance constraints to first order, see Supplementary Section S1.

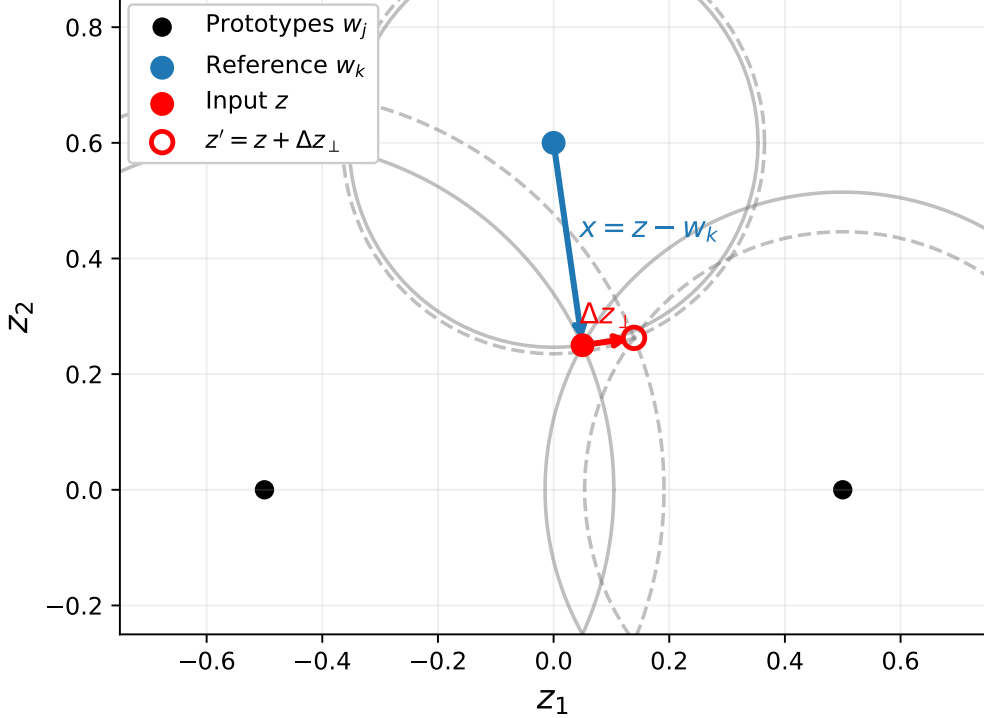


Figure 3: **Radial-tangential decomposition around a reference prototype.** Black dots denote the SOM prototypes  $w_j$ , and the blue point marks the reference prototype  $w_k$ . The red point shows the current input  $z$ , while the unfilled red point indicates the tangentially displaced location  $z' = z + \Delta z_{\perp}$ . The blue arrow represents the radial direction  $x = z - w_k$ , which determines the first-order change of the squared distance to the reference prototype. The red arrow shows a tangential perturbation  $\Delta z_{\perp}$  orthogonal to  $x$  at  $z$ . For each prototype, the solid circle traces the locus of points at the same distance as  $z$ , while the dashed circle shows the corresponding locus for  $z'$ . The circles centered at  $w_k$  coincide at first order, and the circles centered at the other prototypes remain nearly unchanged in the neighborhood of  $z$ , illustrating that tangential motion approximately preserves all squared distances simultaneously.

This decomposition defines a local orthonormal basis aligned with the radial (distance-changing) and tangential (distance-preserving) directions around the prototype  $w_k$ . To control amplitude, we set a total perturbation norm  $r := r_{\text{scale}} \|\Delta z_{\parallel}\|$  and assign

$$\|\Delta z_{\perp}\| = \sqrt{r^2 - \|\Delta z_{\parallel}\|^2}.$$

The resulting perturbation  $\Delta z$  thus combines a controlled radial shift with a tangential adjustment that minimally disturbs the remaining distances. Geometrically, this corresponds to moving the input along the tangent space of the activation manifold in  $\mathbb{R}^N$ , ensuring that the new activation vector  $a(z + \Delta z)$  remains consistent with a realizable point in input space.

The image  $\mathcal{A} = \{a(z) : z \in \mathbb{R}^D\} \subset \mathbb{R}^N$  forms a smooth  $D$ -dimensional embedded submanifold of activation space. By the full-rank Jacobian lemma, the map  $z \mapsto a(z)$  has constant rank  $D$ , so the tangent space at each point  $a(z)$  is  $T_{a(z)}\mathcal{A} = \text{Im } J(z)$  with  $J_j(z) = 2(z - w_j)^\top$ . Since  $\text{rank } J(z) = D$  for all  $z$ , the immersion is regular and  $\mathcal{A}$  has no self-intersections in a neighborhood of each point. Equivalently,  $\mathcal{A}$  can be described implicitly by the quadratic relations among prototypes:

$$a_i(z) - a_j(z) = 2(w_j - w_i)^\top z + \|w_i\|^2 - \|w_j\|^2.$$

Any activation vector  $\tilde{a} \notin \mathcal{A}$  thus violates these consistency relations and cannot correspond to a valid point in  $\mathbb{R}^D$  [24, 25].

Therefore, perturbing a single activation component in isolation generally moves  $a(z)$  outside  $\mathcal{A}$ . To recover a consistent state, the modified activation  $\tilde{a}$  must be reprojected onto  $\mathcal{A}$  by solving the inverse problem

$$\hat{z} = \arg \min_{z \in \mathbb{R}^D} \|a(z) - \tilde{a}\|^2,$$

which reconstructs the closest feasible input configuration realizing the desired activation change [26]. This inversion step ensures that perturbations remain interpretable and respect the geometric structure of the SOM, linking the proposed method to broader ideas of manifold learning and generative topographic mapping ([27, 28, 29]).

However, real data exploration often requires coordinated adjustments involving multiple prototypes or extended trajectories in activation space. Extending the same geometric principle to these cases calls for a regularized formulation that simultaneously enforces attraction toward target activations and preservation of global geometry. This motivates the Manifold–Aware Unified SOM Inversion and Control (MUSIC) framework, which casts activation perturbations as the solution of a Tikhonov–regularized inverse problem balancing attraction and preservation terms.

## 4 The Manifold–Aware Unified SOM Inversion and Control (MUSIC) framework

Building on the geometric constraints identified in the previous section, we now seek a principled way to steer the activation state of a SOM while preserving the consistency of its distance representation in  $\mathbb{R}^D$ . In essence, we aim to translate discrete activation manipulations into continuous, geometry-preserving trajectories in input space, ensuring that every controlled variation remains consistent with the underlying Euclidean embedding. A single-cell perturbation can be analytically described by balancing parallel and orthogonal components of the input displacement. Still, this approach rapidly becomes intractable when multiple prototypes are involved or when one wishes to define continuous, smooth trajectories through the activation manifold [30].

To address these limitations, we introduce the *Manifold–Aware Unified SOM Inversion and Control* (MUSIC) framework—a compact formulation in which all activation-based perturbations of a SOM are expressed as regularized inverse problems. Given a desired change in one or more prototype activations, MUSIC computes the *minimal, geometrically consistent* perturbation of the input vector required to realize this change while remaining aligned with the SOM’s piecewise-linear manifold structure. The term *Manifold–Aware* highlights that the method respects the Voronoi-cell geometry and topological neighbourhoods encoded by the SOM; *Unified* reflects that single-prototype, multi-prototype, and cluster-based transformations all arise from a single quadratic energy; and *SOM Inversion and Control* underscores that the framework inverts activation constraints and uses them as control signals to induce directed, interpretable flows in input space.

At its core, each feasible perturbation  $\Delta z$  is obtained as the solution to a Tikhonov–regularized optimization problem [31] balancing three complementary objectives: (i) the preservation of non–target activations, (ii) attraction toward the desired activation changes, and (iii) a regularization term that enforces smoothness and numerical stability. The resulting update rule admits a closed–form analytical solution, interpretable both geometrically—as a projection in input space weighted by the activation Jacobians—and probabilistically—as the maximum–a–posteriori estimate of a Gaussian Bayesian model [32, 33, 34] (see Supplementary Section S4 for the full probabilistic derivation).

Through this unified energy formulation, MUSIC bridges discrete geometric perturbations and continuous latent–space dynamics, enabling a robust and interpretable exploration of the manifold encoded by the SOM.

### 4.1 Geometric and Topological Analysis of MUSIC Trajectories

MUSIC computes at each iteration a small input perturbation  $\Delta z \in \mathbb{R}^D$  that realizes a desired change in squared–distance activations while preserving the remaining geometry. Let  $a_j(z) = \|z - w_j\|^2$ . Its Jacobian row at  $z$  is

$$J_j(z) = \nabla_z a_j(z)^\top = 2(z - w_j)^\top.$$

Given a preserved index set  $S$  and a target set  $T$ , we form  $A_S$  and  $B_T$  by stacking the rows  $\{J_j(z_t)\}_{j \in S}$  and  $\{J_j(z_t)\}_{j \in T}$ , and apply row normalization  $\hat{J}_j = J_j / \|J_j\|$  to balance per–prototype scale. All Jacobians are evaluated at the current iterate  $z_t$  and updated after each step (periodic relinearization). For a more detailed description of row normalization, refer to Supplementary Section S5.

Intuitively, MUSIC searches for the smallest perturbation  $\Delta z$  that satisfies two antagonistic requirements: it should bring the activations of selected prototypes closer to their target values, while keeping the rest of the activation pattern as unchanged as possible. This trade–off is naturally captured by a quadratic energy function that penalizes deviations in non–target activations and enforces attraction toward the targets. MUSIC chooses  $\Delta z$  as the minimizer of the Tikhonov–regularized quadratic energy (see Supplementary Section S2 for the complete derivation of this energy functional and the justification of the preservation–attraction–regularization balance)

$$E_\gamma(\Delta z) = (1 - \gamma) \|A_S \Delta z\|^2 + \gamma \|B_T \Delta z - b\|^2 + \lambda \|\Delta z\|^2, \quad \gamma \in [0, 1], \lambda > 0, \quad (2)$$

where  $b$  encodes the desired first-order changes of target activations (e.g. for squared distances,  $b$  contains the linearized increments  $\frac{1}{2}\Delta a_t$ ). The normal equations are

$$\left[ (1 - \gamma)A_S^\top A_S + \gamma B_T^\top B_T + \lambda I \right] \Delta z^* = \gamma B_T^\top b. \quad (3)$$

With the shorthand

$$H = (1 - \gamma)A_S^\top A_S + \gamma B_T^\top B_T + \lambda I,$$

we have  $H \succ 0$  for any  $\lambda > 0$ , hence  $E_\gamma$  is strictly convex, guaranteeing a unique minimizer:

$$\Delta z^* = H^{-1} \gamma B_T^\top b.$$

Here the notation  $H \succ 0$  indicates that  $H$  is positive definite, i.e.,  $x^\top H x > 0$  for all nonzero  $x \in \mathbb{R}^D$ . Geometrically, the term  $\lambda \|\Delta z\|^2$  induces an isotropic trust region in the tangent space of the SOM distance manifold, damping motion in directions that are weakly supported by the linearized constraints. The positive definiteness of  $H$  guarantees that each update direction corresponds to a descent step in a locally convex neighborhood of the activation manifold. In practice we enforce a step constraint  $\|\Delta z^*\| \leq \rho$  (or use a line search) and relinearize  $A_S, B_T$  at  $z_{t+1} = z_t + \Delta z^*$ , which keeps the first-order model accurate.

A complementary spectral view is obtained by stacking the constraints as

$$M = \begin{bmatrix} \sqrt{1 - \gamma} A_S \\ \sqrt{\gamma} B_T \end{bmatrix}, \quad y = \begin{bmatrix} 0 \\ \sqrt{\gamma} b \end{bmatrix},$$

so that  $E_\gamma(\Delta z) = \|M\Delta z - y\|^2 + \lambda\|\Delta z\|^2$ . Let  $M = U\Sigma V^\top$  be the SVD with singular values  $\{\sigma_k\}$ . Then

$$\Delta z^* = \sum_k \frac{\sigma_k}{\sigma_k^2 + \lambda} \langle y, u_k \rangle v_k,$$

which shows that  $\lambda$  acts as a spectral low-pass filter: directions with small  $\sigma_k$  (ill-conditioned or conflicting constraints) are attenuated, while well-supported modes pass almost unaltered. This filtering view highlights how MUSIC automatically regularizes ill-posed control problems, acting as a spectral preconditioner that adapts step sizes to the local geometry of the SOM manifold. (A detailed derivation of this spectral form, together with the interpretation of the filter factors and conditioning bounds, is provided in Supplementary Section S3.)

Iterating the update  $z_{t+1} = z_t + \Delta z^*$  yields a discrete trajectory that, in the small-step limit, follows the regularized gradient flow

$$\dot{z} = -\nabla_z E_\gamma(z),$$

with global stability inherited from the strict convexity of  $E_\gamma$ . This connects the inverse-problem formulation to smooth manifold-following dynamics (cf. Riemannian/natural-gradient perspectives [35, 36]). In the limit of infinitesimal steps, the MUSIC dynamics can thus be interpreted as a Riemannian gradient descent on the SOM distance manifold, where the Hessian  $H$  implicitly defines the metric tensor.

In the limit of infinitesimal steps, the MUSIC dynamics can thus be interpreted as a Riemannian gradient descent on the SOM distance manifold, where the Hessian  $H$  implicitly defines the metric tensor.

In applications, MUSIC does not restrict updates to purely tangential directions nor enforce exact isometries of the activation pattern. Each step strikes a balance between (i) modifying the distances in the target set  $T$  and (ii) remaining close to the local tangent space characterized in the geometric analysis, by approximately preserving a subset  $S$  of distances while enforcing Euclidean consistency through an update in  $z$ -space. The tangent-space picture thus serves to describe the geometry of the distance map, while the MUSIC updates exploit this geometry to bias the evolution toward manifold-consistent, semantically meaningful changes rather than exact distance preservation.

The preservation set  $S$  may include either all non-targets or an  $r$ -ring lattice neighborhood around the current BMU, emphasizing local topology preservation. The target set  $T$  can correspond to a single prototype, a predefined cluster, or an informed selection based on semantic similarity. Row weights in  $A_S$  and  $B_T$  may incorporate lattice distances to modulate the influence of neighboring units. Empirically stable trajectories are obtained with  $\gamma \in [0.7, 0.95]$ ,  $\lambda$  chosen via the L-curve criterion [34], and a trust radius  $\rho = 0.02 \|z - w_{\text{BMU}}\|$ .

## 4.2 Exploration modes in MUSIC: free, informed, and cluster control

The MUSIC energy in Eq. (2) can be specialized to three practically important regimes, reflecting different exploration intents: (i) *free* exploration around the current input, (ii) *informed* exploration toward a specific prototype, and (iii) *cluster* exploration toward a set of prototypes. In all cases we work with the linearized operators at  $z_t$ ,

$$J_j(z_t) = 2(z_t - w_j)^\top, \quad A_S = \text{stack}\{\widehat{J}_j : j \in S\}, \quad B_T = \text{stack}\{\widehat{J}_t : t \in T\},$$

with optional row normalization  $\hat{J}_j = J_j / \|J_j\|$  to balance per-prototype scales, and diagonal weights  $W_S, W_T$  (e.g., Gaussian in current distances) to emphasize local topology.

### (i) Free exploration (no explicit target)

Free exploration corresponds to a local random walk on the SOM activation manifold, seeking directions that minimize distortion of the surrounding geometry. It can be thought of as “wandering” in input space while keeping the relative configuration of prototypes nearly unchanged. Formally, this regime captures unconstrained motion along the smooth surface of feasible activations. Since no target prototype is specified, the objective becomes to move in directions that least affect existing distances—those with minimal gradient energy under the local Jacobian field. By following the eigenvectors associated with the smallest eigenvalues of the preservation metric, the algorithm identifies the most neutral, structure-preserving directions available to the input. Adding small Gaussian noise allows the trajectory to explore locally without leaving the valid manifold. Therefore, free exploration seeks small, geometry-preserving moves without enforcing attraction toward any specific prototype.

By removing the target term in Eq. (2) (i.e., setting  $B_T = 0$  and omitting  $b$ ), we obtain the free-exploration regime, where only the preservation and regularization terms remain active. This yields

$$\min_{\Delta z} \|W_S A_S \Delta z\|^2 + \lambda \|\Delta z\|^2 \quad \text{s.t.} \quad \|\Delta z\| \leq \tau. \quad (4)$$

The trivial minimizer is  $\Delta z = 0$ , so one must *choose* a direction in which preserved activations change minimally. Let

$$C = (W_S A_S)^\top (W_S A_S) + \lambda I \succeq 0.$$

Any unit eigenvector  $q_{\min}$  associated with the smallest eigenvalue of  $C$  identifies the *least disruptive* direction. A simple step is then

$$\Delta z^* = \tau q_{\min}, \quad \|\Delta z^*\| = \tau.$$

Stochastic free exploration can be obtained by sampling from the low-eigenvalue subspace of  $C$  (e.g., a few smallest eigenvectors), optionally adding a small radial component toward the current BMU to avoid drift. In practice we relinearize after each step to maintain first-order accuracy.

Table 1: Free exploration with geometry preservation and input-space step noise.

---

**Input:** prototypes  $\{w_j\}_{j=1}^N$ , current point  $z$ , weights  $W_S$ , ridge  $\lambda$ , trust radius  $\tau$ , step-noise scale  $\sigma_z \geq 0$ .

**Output:** updated input  $z'$ .

1. Build  $A_S = \text{stack}\{2(z - w_j)^\top : j = 1, \dots, N\}$  and form  $C = (W_S A_S)^\top (W_S A_S) + \lambda I$ .
2. Compute smallest-eigenvector  $q_{\min}$  of  $C$ .
3. Deterministic step:  $\Delta z_{\text{det}} = \tau q_{\min}$  (or any vector in the low-eigenvalue subspace).
4. Sample noise:  $\xi_z \sim \mathcal{N}(0, \sigma_z^2 I)$  and clip  $\xi_z \leftarrow \min\{1, \tau / \|\xi_z\|\} \xi_z$ .
5. Combine and clip:  $\Delta z = \Delta z_{\text{det}} + \xi_z$ , then  $\Delta z \leftarrow \min\{1, \tau / \|\Delta z\|\} \Delta z$ .
6. Update  $z' = z + \Delta z$  and relinearize at  $z'$ .

---

### (ii) Informed exploration (single target)

Informed exploration introduces a deliberate goal: to move the current input toward a specific prototype while keeping the rest of the map geometrically consistent. It represents a directed but smooth motion, similar to pulling the input toward a known semantic or topological anchor. Here the SOM acts as a controllable field of geometric forces. A target prototype  $t$  exerts a soft attraction proportional to the desired reduction of its distance, while all other prototypes exert a collective regularizing pressure that preserves neighborhood relations. The resulting step is a compromise—partially radial toward  $w_t$  but corrected tangentially to respect the overall manifold curvature. This balance ensures that the evolution remains interpretable and avoids collapsing the map’s topology around a single unit. Hence, informed exploration moves the input toward a chosen prototype  $t \in \{1, \dots, N\}$  while preserving non-target distances to first order.

Let  $T = \{t\}$  and  $S = \{1, \dots, N\} \setminus \{t\}$ . For squared-distance control, set

$$B_T = \hat{J}_t, \quad b = -\eta a_t(z_t) \quad (\eta \in (0, 1]),$$

which requests a fractional reduction of the target activation. The MUSIC step solves

$$\min_{\Delta z} \|W_S A_S \Delta z\|^2 + \gamma \|W_T(B_T \Delta z - b)\|^2 + \lambda \|\Delta z\|^2. \quad (5)$$

The corresponding normal equations are

$$[(W_S A_S)^\top (W_S A_S) + \gamma (W_T B_T)^\top (W_T B_T) + \lambda I] \Delta z^* = \gamma (W_T B_T)^\top (W_T b).$$

This single-target variant recovers the parallel/orthogonal decomposition of Sec. 3 in the limit of vanishing  $\lambda$  and with  $W_S$  projecting onto the local isodistance subspace. Compared to the analytic construction, MUSIC yields a numerically stable, one-shot update that integrates preservation and attraction under a single convex objective.

Table 2: Informed exploration (single target  $t$ ) with target-noise and step-noise.

**Input:** prototypes  $\{w_j\}$ , current  $z$ , target  $t$ , weights  $W_S, W_T$ , penalties  $\gamma, \lambda$ , trust  $\tau$ , fraction  $\eta$ , noise scales  $\sigma_b, \sigma_z \geq 0$ .

**Output:** updated input  $z'$ .

1. Set  $T = \{t\}$ ,  $S = \{1, \dots, N\} \setminus T$ .
2. Build  $A_S, B_T$  from normalized Jacobians  $\hat{J}_j = 2(z - w_j)^\top / \|z - w_j\|$ .
3. Desired change (squared distance):  $b = -\eta a_t(z)$ ; add target-noise  $b \leftarrow b + \xi_b$ ,  $\xi_b \sim \mathcal{N}(0, \sigma_b^2)$ .
4. Solve normal equations:

$$[(W_S A_S)^\top (W_S A_S) + \gamma (W_T B_T)^\top (W_T B_T) + \lambda I] \Delta z_{\text{det}} = \gamma (W_T B_T)^\top (W_T b).$$

5. Sample step-noise  $\xi_z \sim \mathcal{N}(0, \sigma_z^2 I)$ ; set  $\Delta z = \Delta z_{\text{det}} + \xi_z$ .
6. Trust region: if  $\|\Delta z\| > \tau$ , rescale  $\Delta z \leftarrow \tau \Delta z / \|\Delta z\|$ .
7. Update  $z' = z + \Delta z$ ; relinearize and optionally repeat (1–3 passes).

### (iii) Cluster exploration (multi-target)

Cluster exploration generalizes the previous case to coordinated motion toward a group of related prototypes, typically forming a topological or semantic cluster. Rather than aiming at one cell, the trajectory is softly attracted toward an entire region of the map. This regime models high-level transitions between conceptual areas of the SOM. Each prototype in the target set contributes a weighted attraction, producing an aggregate pull toward the cluster's barycentric direction. Simultaneously, distances to all non-target prototypes are preserved, maintaining global geometric coherence. Random sub-sampling of cluster members introduces diversity in the approach path, encouraging smooth blending across overlapping regions and preventing the trajectory from being dominated by a single prototype within the cluster.

Cluster exploration jointly attracts  $z_t$  toward a set  $T$  of prototypes (e.g., a semantic cluster) while preserving distances to the complement  $S = \{1, \dots, N\} \setminus T$ . We build

$$A_S = \text{stack}\{\hat{J}_j : j \in S\}, \quad B_T = \text{stack}\{\hat{J}_t : t \in T\}, \quad b \in \mathbb{R}^{|T|} \text{ with } b_t = -\eta a_t(z_t) \text{ or } b_t = -\eta d_t(z_t),$$

and solve the weighted Tikhonov problem

$$\min_{\Delta z} \underbrace{\|W_S A_S \Delta z\|^2}_{\text{preserve non-targets}} + \gamma \underbrace{\|W_T (B_T \Delta z - b)\|^2}_{\text{shrink targets}} + \lambda \|\Delta z\|^2. \quad (6)$$

Writing  $A_w = W_S A_S$ ,  $B_w = \sqrt{\gamma} W_T B_T$ , and  $b_w = \sqrt{\gamma} W_T b$ , the normal equations are

$$(A_w^\top A_w + B_w^\top B_w + \lambda I) \Delta z^* = B_w^\top b_w. \quad (7)$$

We update  $z_{t+1} = z_t + \Delta z^*$ , enforce a trust radius  $\|\Delta z^*\| \leq \tau$ , and *relinearize* the operators at  $z_{t+1}$ . In practice,  $m = 1\text{--}3$  passes suffice for visibly smooth cluster-consistent motion. When  $T$  is large, Gaussian weights in  $W_T$  (e.g., decaying with current  $d_t(z_t)$ ) emphasize nearby targets and improve conditioning.

Besides sampling multi-element subsets  $T^{(i)} \subseteq T$  at each iteration, we consider a sharper stochastic regime that *randomly selects a single prototype* within the cluster:

$$t^{(i)} \sim \text{Uniform}(T), \quad T^{(i)} = \{t^{(i)}\}.$$

The update is identical to the informed step but restricted to  $t^{(i)}$ , i.e. we solve the Tikhonov subproblem in Eq. (5) with preservation set  $S = \{1, \dots, N\} \setminus \{t^{(i)}\}$  and target set  $T^{(i)}$ . This produces more erratic yet efficient trajectories: by concentrating attraction on one anchor per step while relinearizing, the process explores the cluster region faster and

avoids bias toward the barycentric direction of  $T$ . In expectation (over  $t^{(i)}$ ), the stochastic dynamics approximate the full multi-target control:

$$\mathbb{E}_{t^{(i)}}[\Delta z^*] \approx \arg \min_{\Delta z} \|A_S \Delta z\|^2 + \frac{\gamma}{|T|} \sum_{t \in T} \|A_{\{t\}} \Delta z - b\|^2 + \lambda \|\Delta z\|^2,$$

while reducing per-step cost since only one Jacobian row and one right-hand-side component are active. We refer to this regime as *random informed-within-cluster* exploration.

Table 3: Cluster exploration (multi-target): random target sub-sampling, single-prototype randomization, and noise-augmented updates.

**Input:** prototypes  $\{w_j\}$ , current  $z$ , full target set  $T$ , non-targets  $S$ , weights  $W_T, W_S$ , penalties  $\gamma, \lambda$ , trust  $\tau$ , passes  $m$ , fraction  $\eta$ , sub-sampling rule (size  $k$  or keep-prob  $p$ ), optional single-prototype flag, noise scales  $\sigma_b, \sigma_z \geq 0$ .

**Output:** updated input  $z'$ .

1. Initialize  $z^{(0)} \leftarrow z$ .
2. For  $i = 0, \dots, m - 1$ :
  - a. *Random target selection:*
    - **Multi-target sub-sampling:** draw  $T^{(i)} \subseteq T$  either by fixed size  $|T^{(i)}| = k$  or Bernoulli keep-probability  $p$ .
    - **Single-prototype randomization (optional):** draw a single target  $t^{(i)} \sim \text{Uniform}(T)$  and set  $T^{(i)} = \{t^{(i)}\}$ .
  - b. Build  $A_S^{(i)}, B_{T^{(i)}}^{(i)}$  from local Jacobians at  $z^{(i)}$ ; apply weights  $W_S, W_T$ .
  - c. Desired target changes:  $b_t^{(i)} = -\eta a_t(z^{(i)})$  for  $t \in T^{(i)}$ ; add  $\xi_b^{(i)} \sim \mathcal{N}(0, \sigma_b^2 I)$ :  $b^{(i)} \leftarrow b^{(i)} + \xi_b^{(i)}$ .
  - d. Solve  $(A_w^\top A_w + B_w^\top B_w + \lambda I) \Delta z_{\text{det}}^{(i)} = B_w^\top b_w$ , with  $A_w = W_S^{1/2} A_S^{(i)}$ ,  $B_w = \sqrt{\gamma} W_T^{1/2} B_{T^{(i)}}^{(i)}$ ,  $b_w = \sqrt{\gamma} W_T^{1/2} b^{(i)}$ .
  - e. Sample step-noise  $\xi_z^{(i)} \sim \mathcal{N}(0, \sigma_z^2 I)$  and set  $\Delta z^{(i)} = \Delta z_{\text{det}}^{(i)} + \xi_z^{(i)}$ .
  - f. Trust region:  $\Delta z^{(i)} \leftarrow \min\{1, \tau/\|\Delta z^{(i)}\|\} \Delta z^{(i)}$ .
  - g. Update and relinearize:  $z^{(i+1)} = z^{(i)} + \Delta z^{(i)}$ .
3. Return  $z' = z^{(m)}$ .

All three regimes (free, informed, cluster) share the same convex backbone and differ only by the specification of  $(S, T, W_S, W_T, b)$ . In practice, we solve either the single-target system

$$\left( (W_S A_S)^\top (W_S A_S) + \gamma \hat{J}_t^\top W_T^2 \hat{J}_t + \lambda I \right) \Delta z = \gamma \hat{J}_t^\top W_T^2 b,$$

or the multi-target system in Eq. (7) with a Cholesky factorization (for moderate  $D$ ) or conjugate gradients (for larger  $D$ ). If conditioning deteriorates, one can increase  $\lambda$  or taper the diagonal weights  $W_S, W_T$  (e.g., Gaussian in current distances) to emphasize nearby, better-supported constraints. Free exploration uses the smallest-eigenvalue eigenspace of  $C = (W_S A_S)^\top (W_S A_S) + \lambda I$  as a local exploration metric, yielding least-perturbing directions analogous to metric projection. Informed and cluster exploration instantiate a spectrally filtered least-squares control, where  $\lambda$  damps ill-supported modes and  $\gamma$  sets attraction strength. After each step  $z \leftarrow z + \Delta z$ , we relinearize at the new point to maintain first-order accuracy and enforce a trust radius to keep the linear model valid. In Figure 4, a simple toy model shows the different exploration modes by iterating a small, linearized, Tikhonov-regularized step on the input  $z$ .

To enhance coverage and avoid premature alignment to local geometric modes, we inject small, controlled noise at three safe points: (i) *step noise* in input space, adding  $\xi_z \sim \mathcal{N}(0, \sigma_z^2 I)$  to the deterministic update  $\Delta z$  before trust-region clipping; (ii) *target noise* on the right-hand side, perturbing the desired changes as  $b \leftarrow b + \xi_b$  with  $\xi_b \sim \mathcal{N}(0, \sigma_b^2 I)$ ; and (iii) *gradient jitter* by slightly perturbing the normalized Jacobian rows  $\hat{J}_j \leftarrow \hat{J}_j + \Xi_j$  with small Frobenius norm  $\|\Xi_j\|_F$ . All noises are clipped by the same trust radius to preserve local validity. In the multi-target (cluster) regime, we further promote diversity via *random target sub-sampling*  $T^{(i)} \subseteq T$  at each relinearization pass (either a fixed size  $|T^{(i)}| = k$  or a Bernoulli keep-probability  $p$ ), which empirically improves mixing and reduces bias toward large clusters while keeping the solver and guarantees unchanged.

## 5 Validation and Experimental Analysis

### 5.1 Experimental Strategy and Rationale

To evaluate the proposed inversion and control framework, we designed three complementary experimental setups: synthetic Gaussian mixtures, the MNIST dataset, and the Labeled Faces in the Wild dataset. These experiments are not

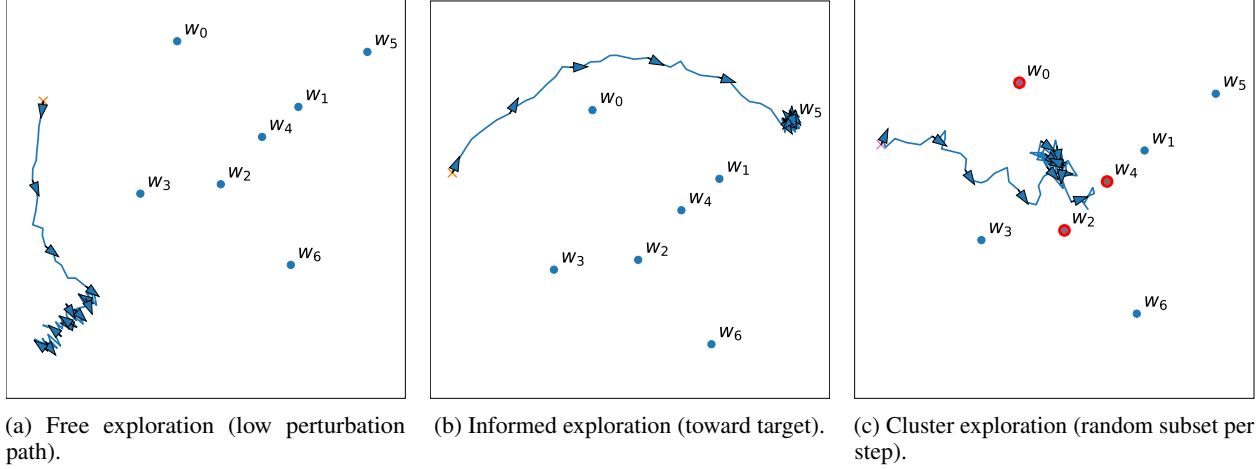


Figure 4: **Exploration modes with consistent activation editing (2D toy).** We place  $n = 7$  prototypes (dots, randomly sampled in  $[-2.5, 2.5]^2$ ) and start from the same point  $z_0$  (cross). Each panel shows a trajectory obtained by iterating a small, linearized, Tikhonov-regularized step on the input  $z$  that (i) preserves non-target activations and (ii) attracts selected targets, with a touch of Gaussian noise per step to emulate exploratory motion. (a) *Free*: the update follows the least-perturbing direction (smallest-eigenvalue eigenvector of  $J(z)^\top J(z)$ ), producing a gentle drift that minimally alters activations. (b) *Informed*: a single target prototype  $w_t$  (hollow circle) is pulled closer by solving  $\min_{\Delta z} \|A_S \Delta z\|^2 + \gamma \|A_T \Delta z - b\|^2 + \lambda \|\Delta z\|^2$ , where  $A_S/A_T$  are the Jacobian rows for preserved/target activations and  $b < 0$  encodes a desired decrease of  $a_t$ . (c) *Cluster*: a cluster  $T$  of prototypes is marked (hollow red circles); at each step we randomly sample a non-empty subset  $T_s \subseteq T$  and apply the same Tikhonov step toward  $T_s$  while softly preserving the rest. Small faint dots indicate a few of the per-step subsets (to avoid clutter). As a lighter variant, at each step we sample a single prototype  $t^{(i)} \in T$  uniformly at random and apply the informed update toward  $t^{(i)}$  while softly preserving the others, yielding more erratic yet efficient coverage of the cluster region. Arrows along the polyline indicate direction. The three regimes visualize, respectively, low-perturbation wandering, targeted attraction, and multi-anchor attraction with stochastic targeting—consistent with the activation-manifold constraints discussed in Sec.3 and the MUSIC formulation in Sec.4.

mere variations of the same procedure; instead, each plays a distinct conceptual role and highlights a different property of the method. Together, they form a progression from controlled geometric validation to semantic interpolation and finally to robustness on real-world perceptual data.

**(1) Gaussian Mixture Models (GMM): Controlled Geometric Validation.** The first experiment establishes the mathematical foundation of our approach in a fully controlled environment. A moderate-dimensional Gaussian Mixture Model (GMM) allows us to isolate and evaluate three core properties:

1. **Invertibility.** We verify that the linear system derived from squared-distance activations yields exact reconstructions once the associated matrix reaches full rank, matching the theoretical requirement  $N \geq D$ . This confirms the identifiability of the SOM activation map under the conditions derived in Section 2.
2. **Stability.** By adding controlled Gaussian noise to the activation layer, we empirically demonstrate the predicted sensitivity scaling

$$\|z - \hat{z}\| \propto \frac{1}{\sigma_{\min}(B)},$$

where  $\sigma_{\min}(B)$  is the smallest singular value of the difference matrix. This reveals that the conditioning of the SOM prototypes—rather than the number of cells alone—governs the stability of the inversion.

3. **Local correctness of MUSIC.** In this noise-free synthetic regime, the Jacobian approximation is highly accurate. We therefore test whether the predicted activation changes  $J\Delta z$  match the true activation changes after a MUSIC update step, validating the local linearization argument at the heart of the method.

This experiment provides the *ground-truth validation* of the proposed framework, independent of semantic or perceptual confounds.

**(2) MNIST: Semantic Structure and Topology-Aware Dynamics.** The second experiment evaluates the method on a real but clean discrete manifold. MNIST offers clear semantic classes, low-level structure, and visually interpretable transformations, making it an ideal benchmark for demonstrating properties that cannot emerge in a synthetic GMM. This experiment highlights:

1. **Semantic interpolation.** MUSIC trajectories between prototypes associated with different digits (e.g. 0 → 1) yield smooth and perceptually meaningful transitions, in contrast to naive pixel or latent-space interpolation.
2. **Topology-aware continuity.** Using the continuity metrics introduced in Section 4, we reveal the characteristic two-scale dynamics of MUSIC on a discrete SOM lattice [2, 37]: (i) locally linear and smooth motion within Voronoi regions, and (ii) sharp but structured reorientations at region boundaries.
3. **Hyperparameter effects.** The parameters  $\gamma$ ,  $\lambda$ , and  $\eta$  modulate the strength of attraction toward the target prototype and the degree of preservation of non-target activations. We show that conservative settings produce stable, coherent deformations, while more aggressive settings accelerate lattice traversal at the cost of increased curvature.

MNIST therefore demonstrates that the geometrically grounded inversion and control mechanisms become *semantically meaningful* when applied to real data.

**(3) Faces in the Wild: Robustness and Perceptual Relevance.** The final experiment tests the method under real-world variability and perceptual complexity. The Labeled Faces in the Wild (LFW) dataset [38] contains large variations in identity, pose, illumination, and expression, and therefore provides a challenging benchmark for assessing robustness.

1. **Robust inversion.** Despite the entangled factors present in unconstrained face images, SOM inversion remains numerically stable, and small perturbations in the activation space correspond to controlled and coherent movements in the embedding space.
2. **Perceptually meaningful control.** MUSIC trajectories produce interpretable transformations in face appearance (e.g. gradual changes in pose, lighting, or expression), demonstrating that the local Jacobian model remains valid on complex perceptual manifolds [39].
3. **Comparison to naive baselines.** Straight-line interpolation in pixel or latent space often generates unnatural distortions or off-manifold images. In contrast, MUSIC maintains on-manifold structure, showing clearer and more controllable attribute variation.

This experiment demonstrates that the proposed method generalizes beyond toy datasets and remains effective on challenging, high-dimensional visual data.

## 5.2 Continuity and Topology-Aware Metrics

To characterize the dynamical behavior of MUSIC trajectories across different datasets, we employ a set of continuity and topology-aware metrics. These quantities capture complementary aspects of the motion induced by the control updates, ranging from fine-grained local smoothness to large-scale geometric coherence. Because Self-Organizing Maps (SOMs) define a piecewise-linear partition of the input space, with Voronoi regions governed by individual prototypes, trajectory analysis must account for both continuous evolution within a region and discrete reorientations at region boundaries. The following metrics provide a comprehensive description of these phenomena and will be used throughout all experimental setups.

**Step-direction continuity.** A first measure of local smoothness is the cosine similarity between consecutive update directions,

$$C_t = \frac{\langle \Delta z_t, \Delta z_{t+1} \rangle}{\|\Delta z_t\| \|\Delta z_{t+1}\|}, \quad \Delta z_t = z_{t+1} - z_t.$$

Values  $C_t \simeq 1$  indicate nearly collinear updates, whereas smaller or negative values reveal local directional reorientations.

**Topology-aware continuity.** Because a SOM induces a piecewise-linear tiling of the input space [2, 37], longer trajectories may cross the boundaries between Voronoi regions associated with different prototypes. At each crossing, the Jacobian structure changes and the optimal update direction is reoriented. To separate smooth evolution within a region from abrupt changes caused by boundary crossings, we evaluate all continuity metrics in a *topology-aware* manner conditioned on the evolution of the best-matching unit (BMU).

**Transition rate.** The *transition rate* quantifies how frequently the BMU changes along the path:

$$r_{\text{trans}} = \frac{1}{T} \sum_{t=0}^{T-1} \mathbf{1}[\text{BMU}(z_{t+1}) \neq \text{BMU}(z_t)].$$

Low values correspond to motion within a single basin of attraction; higher values reflect lattice traversal and frequent region crossings.

**Dwell statistics.** Between two transitions, the trajectory remains associated with the same prototype. The number of consecutive steps spent within a region defines a *dwell length*  $L_k$ . The median and interquartile range (IQR) of the set  $\{L_k\}$  quantify the stability of residence within topological cells: longer dwell times correspond to stable local exploration, while short dwell times indicate rapid hopping between prototypes.

**Curvature.** The angular deviation between successive directions,  $\theta_t = \cos^{-1}(C_t)$ , provides a notion of local curvature. We normalize this by the step length to obtain the curvature per unit step,

$$\kappa_t = \frac{\theta_t}{\|\Delta z_t\|}.$$

We report median curvature separately for within-cell motion ( $\kappa_{\text{within}}$ ) and across-cell transitions ( $\kappa_{\text{trans}}$ ). Large  $\kappa_{\text{trans}}$  indicates the sharp reorientations produced at Voronoi boundaries.

**Geodesic efficiency.** To assess global coherence, we compare the total path length with the direct displacement between start and end points:

$$E_g = \frac{\|z_T - z_0\|}{\sum_{t=0}^{T-1} \|\Delta z_t\|}.$$

A value  $E_g = 1$  corresponds to a perfectly straight trajectory, while smaller values indicate folded or meandering paths. Geodesic efficiency thus complements local metrics by quantifying long-range smoothness.

**Segmented continuity.** Finally, for each dwell segment (i.e., the interval between two BMU transitions), we compute the average step-direction continuity  $\bar{C}_k$ . The distribution of  $\{\bar{C}_k\}$  captures the internal coherence of motion within stable regions. We report its median and interquartile range to characterize the variability of local behavior along the trajectory.

All continuity-based metrics (step continuity, curvature, geodesic efficiency, and segmented continuity) are unitless and invariant under uniform rescaling of the step sizes.

### 5.3 Synthetic validation on Gaussian mixture models

We first assess the proposed inversion and interpolation mechanisms in a controlled setting where both the data distribution and the prototype geometry are explicitly known. We consider a three-component Gaussian Mixture Model (GMM) in  $\mathbb{R}^D$  (here  $D = 10$ ), whose component means forming a triangle in the first two coordinates, while the remaining dimensions contain small isotropic noise. From 25,000 samples we train a rectangular  $20 \times 20$  SOM; an independent test set of 8,000 points is standardized using the same statistics. All experiments in this subsection operate directly in the standardized space.

Given a test point  $z$  and its best-matching prototype  $r$ , the inversion procedure constructs the anchored linear system  $Bz = c$  from squared-distance activations (Section 2.1), where each row of  $B$  encodes an affine difference between prototype  $r$  and another prototype. Using a subset of  $N$  prototypes yields an  $N \times D$  system. For each test point and for  $N \in \{1, \dots, N_{\text{max}}\}$ , we form the least-squares estimate  $\hat{z} = B^+ c$  and record the reconstruction error  $\|z - \hat{z}\|_2$ . Theory predicts that inversion is unstable when  $N < D$  (under-determined system) and becomes exact as soon as  $B$  attains full column rank, i.e., once the selected prototypes span a  $D$ -dimensional affine subspace.

Figure 5 shows the median error across 1,500 test points as  $N$  increases. The error remains large and slowly decreasing for  $N < D$ , then drops abruptly to numerical zero at  $N = D$  and stays there for all  $N > D$ . This provides a direct empirical confirmation that the distance-based linear system is essentially lossless once a full-rank set of prototypes is used.

Beyond static inversion, the same GMM setting also allows us to study the *dynamics* induced by MUSIC in a structured, multi-modal manifold. On this triangular mixture, the trained SOM organizes its prototypes into three regions aligned with the mixture components. We then examine two complementary trajectory regimes:

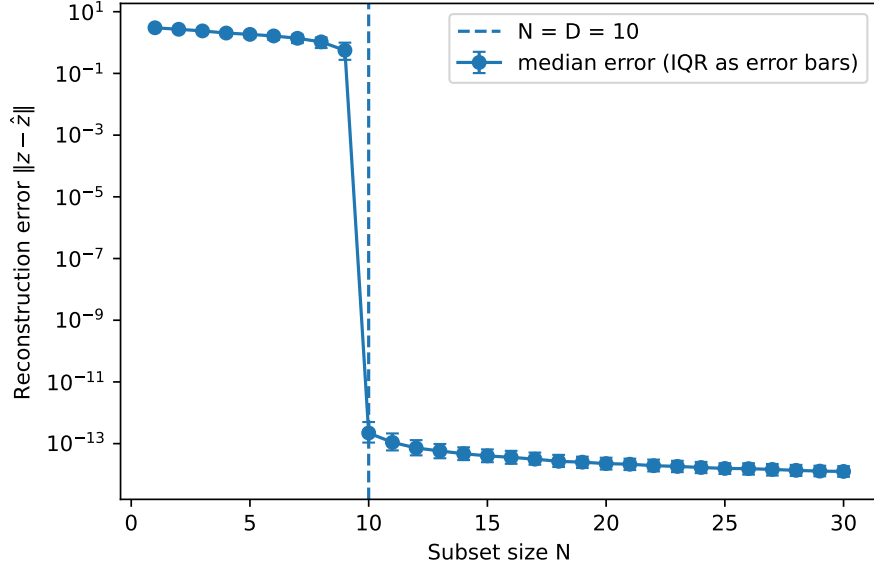


**Figure 5: Inversion accuracy on a Gaussian mixture.** Median reconstruction error  $\|z - \hat{z}\|_2$  as a function of the subset size  $N$  used to build the anchored system  $Bz = c$  from squared-distance activations. A  $20 \times 20$  SOM is trained on a  $D = 10$  GMM; errors are averaged over 1,500 test points, with error bars denoting the interquartile range. The dashed vertical line marks the intrinsic dimension  $D$ . In line with the theoretical analysis, inversion is unstable for  $N < D$  but collapses to machine precision at  $N = D$ , and remains at the numerical floor for all overdetermined systems  $N > D$ , confirming that squared activations carry enough geometric information to recover the input uniquely.

**(a) Informed convergence toward a single prototype.** In the first regime, all trajectories are attracted toward a fixed SOM prototype chosen near the mean of one GMM component. Initial states are sampled from all three clusters, so starting points are topologically diverse. The MUSIC update rule generates sequences that move toward the selected prototype (with optional small Gaussian noise). Despite crossing multiple Voronoi boundaries, trajectories remain locally smooth with low within-cell curvature and converge to the same attractor, illustrating a globally coherent flow capable of targeting isolated semantic anchors.

**(b) Local exploration of a cluster-specific neighbourhood.** In the second regime, the target at each step is chosen at random among the prototypes belonging to a selected cluster. Trajectories again start from all three mixture components: they are first pulled into the corresponding prototype region and then wandered within it, showing short dwell lengths, frequent BMU transitions, and moderate curvature. This behavior reflects a multi-scale organization: MUSIC guides points into the appropriate semantic basin at a global scale, while locally it induces piecewise-linear exploration constrained by the SOM topology.

To complement the qualitative trajectory plots, we report in Table 4 a set of global scalar metrics that summarize the behaviour of MUSIC dynamics on the GMM manifold. We focus on the topology-aware measures defined in Section 5.2: transition rate, dwell statistics, step-direction continuity, curvature, geodesic efficiency, and segmented continuity.

The metrics reveal a clear contrast between the two dynamical regimes. In the informed-convergence setting, the transition rate is low and dwell times are long, reflecting coherent motion within stable Voronoi regions. Step-direction continuity remains high and geodesic efficiency is close to 1, indicating globally directed flow toward the designated prototype. In the cluster-exploration regime, transitions are frequent and dwell times shrink to one or two steps. Continuity decreases, curvature becomes more variable, and geodesic efficiency drops substantially, consistent with locally wandering, topology-constrained motion within the selected mixture component. Together, these experiments show how MUSIC behaves on a simple multimodal manifold: through *directed* convergence to a single prototype and *exploratory* motion confined to a cluster-specific region. Both behaviours will reappear, in less controlled form, when we move to real datasets.

Having validated the inversion mechanism and characterized MUSIC dynamics in a controlled multimodal environment, we now turn to a real image manifold where both topology and semantic structure emerge directly from the data, rather than being prescribed.

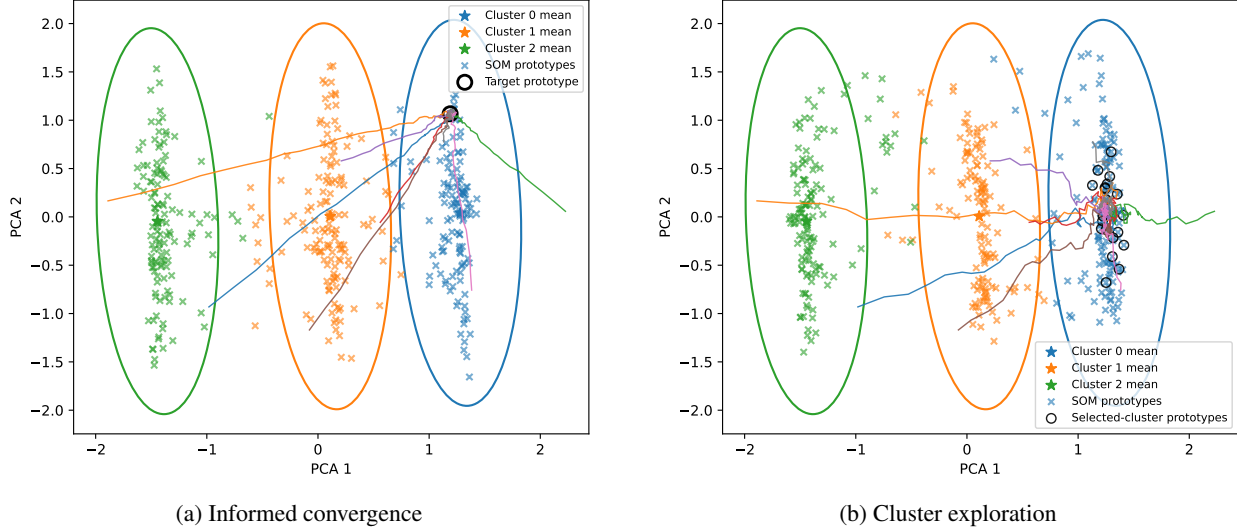


**Figure 6: Trajectory behavior on a three-cluster GMM manifold.** A SOM is trained on a triangular GMM, yielding three prototype regions (colours indicate assignment to the nearest mixture component). **(a)** MUSIC trajectories initialized from all clusters converge toward a single target prototype (circled), following smooth paths with low curvature even across Voronoi boundaries. **(b)** When the target at each step is sampled randomly from the prototypes of one cluster, trajectories are first attracted into that mode and then follow short, piecewise-linear exploratory segments within it. Ellipses show the  $2\sigma$  covariance contours of the three GMM components.

Metric	Median $\pm$ IQR
Transition rate $r_{\text{trans}}$	$0.042 \pm 0.021$
Dwell length (steps)	$6.0 \pm 10.25$
Dwell IQR	$17.38 \pm 12.50$
Step–direction continuity $C$	$0.291 \pm 0.093$
Curvature $\kappa$	$34.86 \pm 7.12$
Geodesic efficiency $E_g$	$0.757 \pm 0.089$
Segmented continuity $\bar{C}_k$	$0.944 \pm 0.362$
Segmented continuity IQR	$0.364 \pm 0.188$

(a) Informed convergence

Metric	Median $\pm$ IQR
Transition rate $r_{\text{trans}}$	$0.383 \pm 0.100$
Dwell length (steps)	$1.5 \pm 1.13$
Dwell IQR	$1.75 \pm 1.44$
Step–direction continuity $C$	$0.079 \pm 0.274$
Curvature $\kappa$	$9.42 \pm 0.93$
Geodesic efficiency $E_g$	$0.291 \pm 0.059$
Segmented continuity $\bar{C}_k$	$-0.007 \pm 0.328$
Segmented continuity IQR	$0.475 \pm 0.165$

(b) Cluster exploration

**Table 4: Quantitative analysis of MUSIC trajectories on the GMM manifold.** Each entry reports the median  $\pm$  IQR across trajectories. **(Left)** Informed convergence: trajectories exhibit low transition rate, long dwell times, higher global step–direction continuity, and high geodesic efficiency, indicating globally directed motion toward a single prototype. **(Right)** Cluster exploration: trajectories undergo frequent BMU transitions, short dwell times, lower continuity, and reduced geodesic efficiency, reflecting locally wandering, topology-constrained exploration within the selected mixture component.

#### 5.4 Experiments on MNIST

We now examine MUSIC on real-world data, moving from the controlled structure of the GMM to a high-dimensional image manifold whose topology and semantic organization must be learned directly from the samples. We train a  $32 \times 32$  toroidal SOM on the MNIST handwritten digit dataset [40] after full-dimensional PCA whitening. The toroidal topology avoids boundary artefacts and forces all classes to be embedded in a common continuous latent surface. The resulting map forms a two-dimensional lattice of prototypes whose spatial arrangement reflects the class structure of handwritten digits. By assigning each prototype the majority label of its BMU matches, we obtain ten coherent prototype regions corresponding to the ten digit classes.

This setting provides a first realistic test of the inversion and interpolation mechanisms introduced in the previous sections. MNIST offers a compact yet semantically rich manifold: intra-class variations are smooth and low-dimensional, while inter-class boundaries are sharp. A SOM captures these structures through a spatially contiguous prototype



Figure 7: **Prototype organization on MNIST.** A  $32 \times 32$  toroidal SOM trained on PCA–whitened MNIST forms ten coherent prototype regions corresponding to the digit classes. Neighbouring prototypes capture smooth morphological variations, while class boundaries emerge along contiguous regions of the map.

neighbourhoods, making MNIST an ideal benchmark for assessing the quality of MUSIC trajectories, their continuity properties, and their ability to traverse latent space in a class–aware manner. In the following experiments, we investigate how inversion behaves on this learned manifold, how MUSIC interpolations evolve within and across classes, and how these dynamics differ from those observed in the synthetic GMM setting.

#### 5.4.1 Prototype organization on MNIST

We begin by examining the organization of the SOM trained on the PCA–whitened MNIST dataset. The resulting lattice contains 1024 prototypes arranged on a two-dimensional grid that captures the semantic structure of handwritten digits. For each prototype, we assign a class label based on the majority of the training data samples for which it is the best-matching unit (BMU). This produces ten spatially coherent regions corresponding to the ten digit classes.

Neighbouring prototypes within each region represent smooth morphological variations of the same digit, such as differences in stroke thickness, orientation, or style. Transitions between digit classes occur along contiguous boundaries where prototype basins meet. This topological structure provides a meaningful latent geometry on which MUSIC trajectories operate: class regions act as locally smooth domains, while their interfaces define natural transition surfaces for cross–class evolution.

Figure 7 illustrates the resulting prototype map, with colours indicating class assignments and thumbnails showing the corresponding prototype images.

#### 5.4.2 Inversion behaviour on MNIST

Before analysing MUSIC trajectories, we verify that the inversion mechanism derived in Section 2.1 remains numerically stable on real data. For each MNIST test image, we compute squared–distance activations from the SOM prototypes, form the anchored system  $Bz = c$ , and recover  $\hat{z} = B^+c$ . Because the map contains many more than  $D$  prototypes, and they span the whitened PCA space in a general position, the resulting systems are highly overdetermined. Consequently, reconstruction errors  $\|z - \hat{z}\|_2$  are consistently near machine precision. This guarantees that intermediate MUSIC states, many of which do not correspond to real training images, can still be faithfully decoded back into pixel space.

#### 5.4.3 Directed class transition

We first analyse a cross–class MUSIC interpolation starting from an input image of the digit “0” and directing the trajectory toward a prototype representing the digit “1”. The resulting path illustrates the semantic structure learned by the SOM (Fig. 8). Initially, the updates deform the “0” while preserving its circular outline. As the trajectory approaches

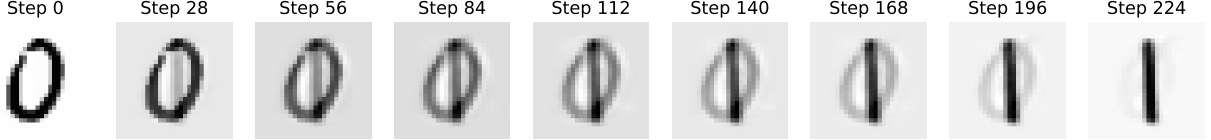


Figure 8: **MUSIC trajectory from “0” to “1” on MNIST (Tikhonov variant).** Starting from a test image of the digit “0” (left), MUSIC is run in informed mode toward a target prototype representing the digit “1” (right) using the Tikhonov-regularized update rule. The intermediate reconstructions exhibit a smooth and interpretable evolution: the circular stroke of the “0” gradually fades while a vertical segment progressively appears and sharpens. Around the middle of the path, both structures are partially visible, forming a hybrid configuration that reflects the proximity of the two class regions on the SOM. As the trajectory enters the “1” region, the loop disappears entirely and the representation stabilizes into a clean “1”. These intermediate states result from topology-aware latent updates rather than pixel-space interpolation, and the Tikhonov formulation yields a particularly stable, smooth transition.

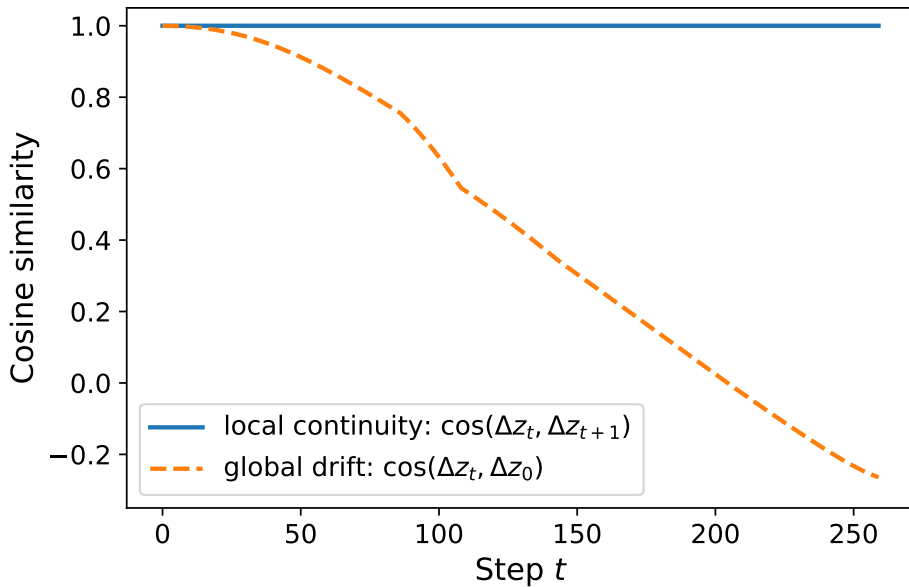


Figure 9: **Step–direction continuity on the MNIST “0”→“1” transition.** We report the cosine similarity between successive update directions,  $\cos(\Delta z_t, \Delta z_{t+1})$ , and between each update and the first one,  $\cos(\Delta z_t, \Delta z_0)$ , along the informed trajectory. The high local similarity (solid line) shows that consecutive steps remain nearly collinear, confirming the smoothness of MUSIC updates in the latent space. The gradual decay of global similarity (dashed line) reflects the expected reorientation of the trajectory as it crosses multiple Voronoi regions on the SOM while moving from the “0” manifold toward the “1” prototype. Together, these curves quantify the locally coherent yet globally bending nature of the MUSIC flow on a real data manifold.

the boundary between the “0” and “1” prototype regions, a hybrid configuration emerges: the loop becomes fainter while a vertical stroke begins to appear. This intermediate state reflects the geometry of the SOM, where the two class basins meet. After crossing the boundary, the trajectory aligns with the “1” region and converges smoothly toward the target prototype.

To quantify the smoothness of the latent trajectory beyond visual inspection (Fig. 9), we compute cosine similarities between successive update directions,  $\cos(\Delta z_t, \Delta z_{t+1})$ , and between each update and the initial direction,  $\cos(\Delta z_t, \Delta z_0)$ . These two measurements capture complementary aspects of MUSIC dynamics. The first remains consistently close to 1 throughout the trajectory, indicating that consecutive steps are almost perfectly aligned and the motion is locally smooth. The second decreases steadily as the trajectory progresses, revealing a gradual reorientation of the update direction as the path crosses several Voronoi boundaries on the SOM. The joint behaviour of these curves illustrates the expected two-scale structure of MUSIC: locally coherent, low-curvature motion governed by the piecewise-linear geometry of the SOM, together with a global bending of the trajectory as it moves from the “0” region toward the “1” prototype.

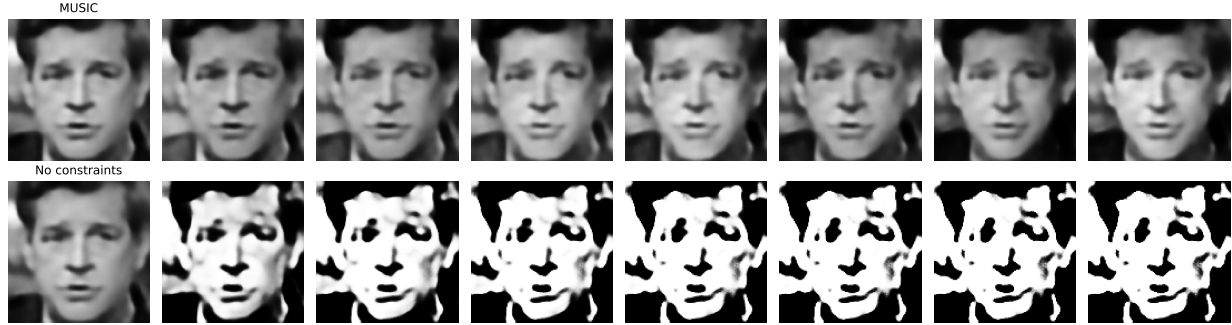


Figure 10: **Free evolution in latent space under geometry-aware control.** Starting from the same input face (left), we repeatedly apply random perturbations to the squared distance of a randomly selected SOM prototype. In the *MUSIC* row (top), each perturbation is processed through manifold-aware inversion: the update direction is chosen to satisfy the perturbed distance while preserving a small subset of nearby prototype distances, and the resulting step is normalized to a fixed magnitude. In the *no-constraints* row (bottom), the latent update is taken along the purely radial direction of the selected prototype, with the same step length but without any geometric preservation. Despite identical latent step sizes, the unconstrained trajectory rapidly drifts off the face manifold and produces distorted images, whereas MUSIC yields smooth, semantically coherent transformations that preserve the overall facial structure.

This example highlights the interpretability of MUSIC dynamics: intermediate states are meaningful, structured, and reflect the local geometry of the learned manifold rather than producing arbitrary linear blends of images.

### 5.5 Experiments on Faces in the Wild

After evaluating MUSIC on synthetic data and handwritten digits, we now examine its behavior on a high-dimensional, real-world visual manifold. We use a “Faces in the Wild” dataset [38], encode each image into a 512-dimensional latent vector via a pretrained autoencoder, and apply PCA whitening. A  $32 \times 32$  SOM trained on these latent codes organizes faces according to broad semantic attributes—gender, skin tone, hairstyle, facial structure, and illumination—yielding a rich topological landscape suitable for controlled semantic explorations.

To illustrate the semantic benefits of geometry-aware inversion, we perform a free-evolution experiment starting from the same reference face. At each step, we randomly select a SOM prototype and impose a random perturbation of its squared distance. In the *MUSIC* condition, the update direction is obtained via our manifold-consistent inversion (preserving a small set of distances while driving the selected one), and the latent step is normalized to a fixed magnitude. In the *no-constraints* baseline, the latent update is instead taken along the purely radial direction of that prototype, without any geometric preservation.

Although both trajectories have identical step lengths in latent space, their qualitative behaviour differs drastically. The unconstrained trajectory rapidly drifts into implausible regions of latent space, yielding distorted faces. In contrast, the MUSIC trajectory evolves smoothly and remains on the face manifold, exhibiting coherent semantic transformations such as changes in expression, illumination, or local attributes without collapsing into artifacts. Figure 10 shows a representative example. This identity preservation is a distinctive advantage of MUSIC compared to unconstrained latent interpolations or direct attribute-transfer methods. For a more detailed description of this experiment, refer to Supplementary Section S6.

Beyond these local transformations, MUSIC also exhibits a structured global behavior: when iterated with consistent prototype selections, the latent trajectory converges toward the corresponding cluster. In this case, MUSIC is run in *informed mode*, where at each step the update direction is defined by a single prototype selected from a user-chosen target cluster. This one-prototype-at-a-time guidance is crucial on high-dimensional data: while cluster-based forcing tends to introduce instability, the informed mode produces smooth, realistic, and decoder-faithful trajectories that remain close to the learned manifold.

A central property of informed MUSIC on faces is that the identity of the starting image is largely preserved throughout most of the trajectory. Because each update step is guided by a real SOM prototype and constrained by the local geometry of the map, the latent state remains close to the region representing the original face. Attributes such as skin tone, facial softness, or local photometric features evolve gradually, but core identity cues remain stable until the trajectory approaches the target region. This identity preservation is a distinctive advantage of MUSIC compared to unconstrained latent interpolations or direct attribute-transfer methods.

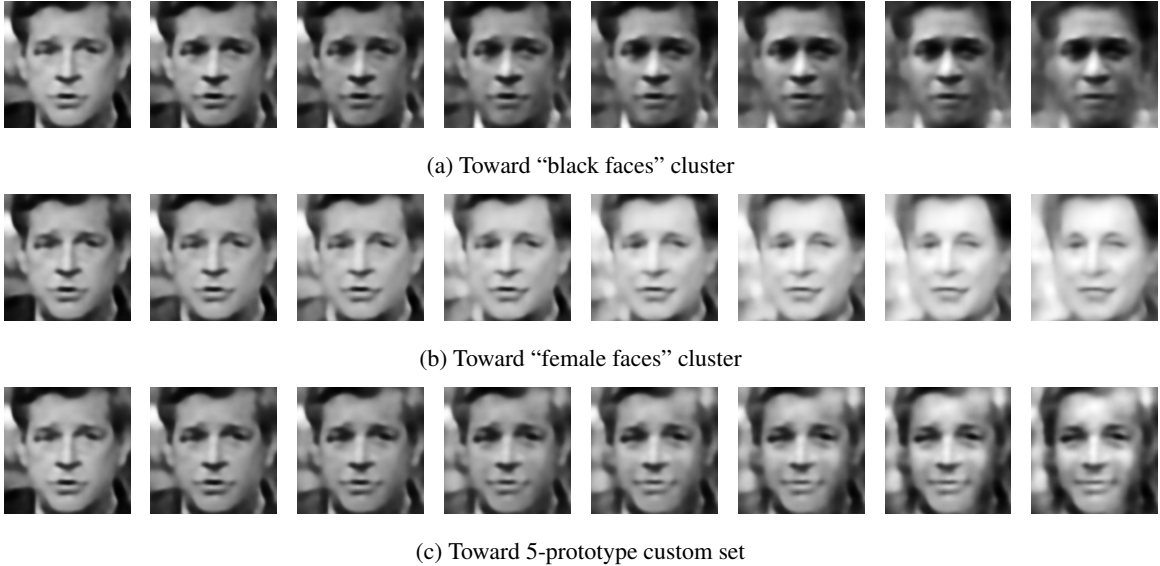


Figure 11: **MUSIC informed explorations on the facial manifold.** Starting from the same validation image (leftmost column), MUSIC moves along smooth, semantically meaningful directions induced by SOM topology. Each trajectory is guided by repeatedly selecting a single prototype from the target set. The input face is taken from the held-out validation set and was not used during SOM training.

We illustrate three types of explorations, each probing a distinct semantic direction on the SOM (see Fig. 11):

**(a) Transition toward a demographic region.** Starting from a validation image, we guide the trajectory toward a cluster containing predominantly darker-skinned faces. The evolution shows a smooth darkening of skin tone and gradual adjustments in local shading and facial texture. Identity remains stable deep into the trajectory, indicating that MUSIC follows a coherent semantic direction encoded in the map.

**(b) Transition toward a gender-specific region.** Using the same initial face, we target a cluster of mainly female prototypes. The resulting path progressively introduces features associated with the cluster—subtle changes in eyes, eyebrows, and facial softness—again without introducing abrupt distortions. The evolution reflects the geometry of the learned manifold rather than performing direct attribute transfer.

**(c) Convergence toward a small user-defined prototype set.** To test MUSIC in a minimally constrained setting, we select a set of only five prototypes at random (not forming a labelled cluster) and use them as informed anchors. The trajectory remains stable and interpretable: the face moves toward a mixed semantic region combining attributes of the selected prototypes. This highlights a key strength of MUSIC: coherent transformations can be driven even by small, unlabeled sets of latent anchors.

To quantitatively verify that informed trajectories reach their intended semantic regions, we measure—for the experiment targeting the “female” cluster—the mean Euclidean distance between the latent state  $z_t$  and all prototypes in that cluster. As shown in Fig. 12, the distance decreases smoothly and monotonically, confirming that the latent dynamics consistently move toward the target region rather than merely generating plausible intermediate faces. Similar behaviours are observed for other transitions.

For the simple case of moving from a single face to a single target prototype, we also consider a baseline given by straight linear interpolation in the 512-dimensional latent space between the two endpoints. In this regime, MUSIC and linear interpolation produce very similar trajectories, indicating that, along this direction, the autoencoder latent space is already close to being locally Euclidean, and the SOM prototypes lie roughly on a straight semantic path. We therefore view this setting as a sanity check of consistency rather than a regime where MUSIC is expected to offer a decisive advantage.

To further probe the behaviour of MUSIC relative to standard latent-space operations, we evaluate a stronger baseline in which the starting face is compared not to a single target prototype but to an entire semantic cluster—specifically, the same female-faces cluster used in the informed MUSIC experiment. For MUSIC, we retain the informed mode: at each

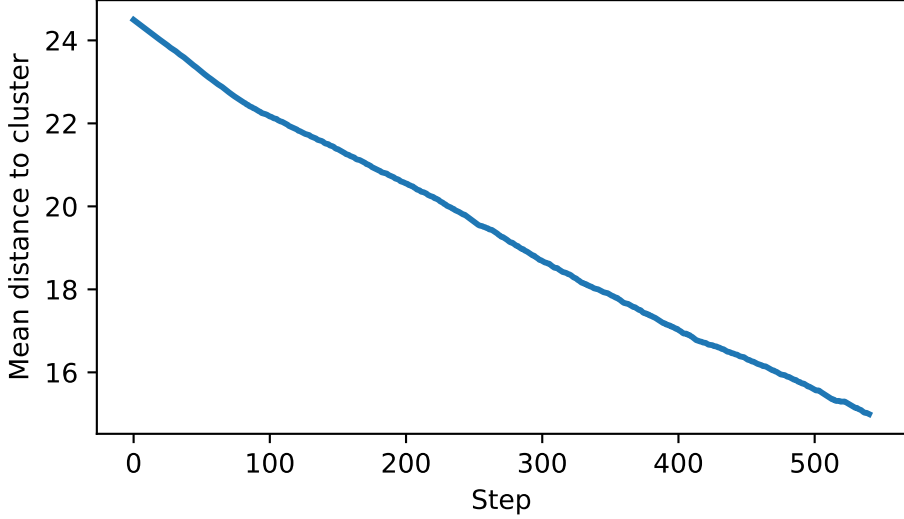


Figure 12: **Convergence toward the target prototype cluster.** Mean Euclidean distance between  $z_t$  and the “female” cluster prototypes along the trajectory of Fig. 11(b). The monotonic decay confirms directed motion toward the target region.

step, the latent update is directed toward a single randomly selected prototype from the target cluster, ensuring that every intermediate state remains anchored to a valid SOM codebook vector. For the baseline, we construct the standard linear path from the initial latent point to the mean of all prototypes in the target cluster.

This comparison isolates two fundamentally different mechanisms:

Linear interpolation moves straight toward the cluster barycenter, effectively averaging all facial features in the group. This produces increasingly blurred and identity-agnostic faces as interpolation progresses.

Informed MUSIC, instead, follows a piecewise-smooth trajectory guided by actual prototypes. The path bends across Voronoi regions, but every intermediate point remains close to a real face embedding, preserving essential structure and identity characteristics until later in the transition.

Figure 13 illustrates these effects visually. Although both paths start from the same validation image and aim toward the same semantic target, the linear interpolation collapses rapidly into a blurry, homogenized representation dominated by the mean appearance of the cluster. By contrast, the MUSIC trajectory produces sharper and more realistic intermediate faces, with the original identity clearly preserved deep into the sequence. Only near convergence do the characteristic attributes of the target cluster become dominant.

These qualitative differences are reflected quantitatively in the two accompanying metric plots (Fig. 14). The left panel reports the mean Euclidean distance between the latent point and the target cluster. Linear interpolation reduces this distance aggressively—from roughly 25 down to nearly 3—because the cluster mean lies extremely close to many prototypes, acting as a geometric attractor. MUSIC, by contrast, converges more moderately—from 25 to 15—reflecting its tendency to follow the cluster’s semantic envelope rather than collapsing into its barycenter.

The right panel shows the identity drift, measured as the deviation of squared distances from the identity-anchor prototypes, which are fixed around the initial BMU. Here, the difference between the two methods is striking: MUSIC maintains almost perfect identity preservation (drift  $\approx 0$  to 10) throughout most of the trajectory, indicating that the transformation remains semantically controlled. Linear interpolation, however, causes identity to deteriorate rapidly—with drift climbing to nearly 800 by step 250—before slightly decreasing near the very end.

Together, these comparisons highlight the core distinction between the two approaches. Linear paths tend to leave the data manifold in the direction of a blurred “cluster average,” even when the autoencoder latent space is smooth. MUSIC produces transitions that remain sharp, interpretable, and close to the manifold structure enforced by the SOM prototypes, preserving the defining attributes of the starting face while still moving toward the desired semantic region.

For reproducibility, and to avoid result-specific parameter tuning, all experiments on faces were performed using a single fixed configuration of MUSIC hyperparameters ( $\gamma = 0.85$ ,  $\lambda = 10^{-4}$ ,  $\rho = 0.1$ ,  $\eta = 0.04$ ,  $\sigma = 0.01$ ). This



Figure 13: **MUSIC vs. linear interpolation toward a target facial cluster.** MUSIC (top row) preserves identity and produces sharp intermediate faces, while linear interpolation (bottom row) collapses toward a blurred cluster mean. Both trajectories target the female-faces cluster.

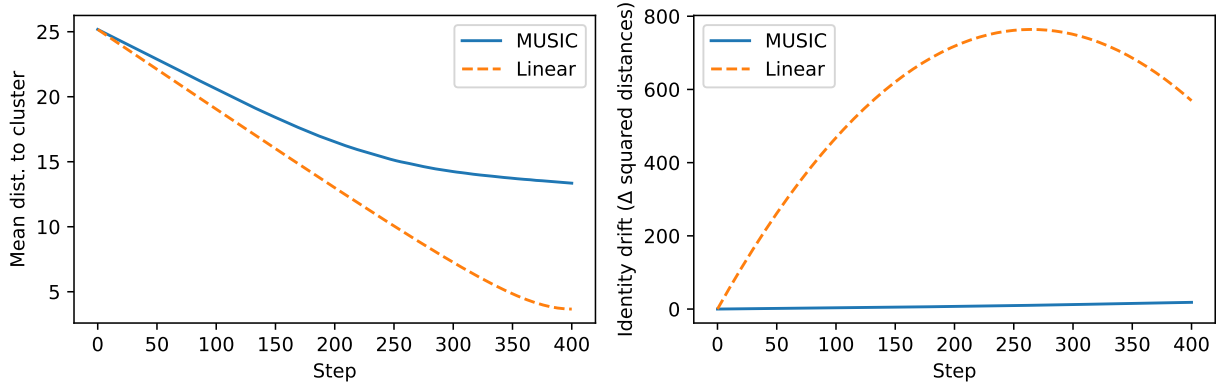


Figure 14: **Convergence and identity drift during MUSIC vs. linear transition.** (Left) Mean distance to the female-faces cluster. Linear interpolation collapses to the cluster barycenter, while MUSIC approaches the cluster more conservatively. (Right) Identity drift relative to initial anchors. MUSIC preserves identity for most of the trajectory, whereas linear interpolation causes a dramatic loss (up to  $\sim 800$ ) before partially recovering near its endpoint.

guarantees that the observed behaviours—smooth transitions, cluster convergence, and identity preservation—arise from the method itself rather than from per-sample adjustment.

Overall, these experiments demonstrate that MUSIC remains stable and semantically meaningful on a highly nonlinear manifold of real faces. Compared to digits or synthetic data, facial images involve complex entanglement of identity, pose, illumination, and demographic attributes. Despite this complexity, informed MUSIC trajectories perform long-range semantic transitions while preserving photometric consistency and remaining within the domain of valid decoder embeddings. This bridges controlled geometric validation with realistic visual data, highlighting SOM inversion as an effective tool for interpretable exploration of latent spaces.

## 6 Discussion

A central insight of this work is that the structure of the prototype set plays a crucial role in the stability and interpretability of the resulting trajectories. While the inversion mechanism requires only  $N \geq D+1$  affinely independent vectors, the behaviour of MUSIC depends strongly on how these reference points are organized in space. If prototypes are sampled randomly or obtained from unstructured clustering, the resulting Voronoi cells have no coherent semantic geometry: neighbourhoods do not correspond to gradual attribute changes, boundary transitions occur abruptly, and intermediate states are difficult to interpret. In such settings, MUSIC produces unstable or chaotic motion because the underlying partition lacks topological meaning.

In contrast, a Self-Organizing Map provides a two-dimensional, topology-preserving lattice in which neighbouring prototypes correspond to semantically similar inputs. This induces smooth Voronoi regions and contiguous boundaries that together form a piecewise-linear coordinate chart of the data manifold. MUSIC leverages precisely this structure:

within a single region, the Tikhonov-regularized flow produces low-curvature motion aligned with local prototype geometry, while boundary crossings occur in a predictable manner reflecting the lattice topology. This behaviour cannot be replicated by standard clustering methods such as  $k$ -means or  $k$ NN grouping, which lack neighbourhood continuity and provide no global topological backbone for guiding semantic transformations.

Viewed from this perspective, MUSIC offers a deterministic, geometry-driven mechanism for semantic interpolation that complements modern generative models. Whereas VAEs or diffusion models define trajectories through neural parameterization or stochastic sampling, MUSIC defines them through prototype geometry and linear algebra alone. This provides a high degree of interpretability: transformations remain anchored to real prototypes, boundary transitions correspond to explicit geometric events, and the flow never relies on decoder priors or latent stochasticity.

A comparison with linear interpolation in the autoencoder latent space further clarifies the behaviour of MUSIC. When moving between a single face and a single target prototype, both linear and MUSIC trajectories behave similarly, confirming that in such simple directions the latent space is locally close to Euclidean. More informative differences appear when moving toward an entire semantic cluster: straight-line interpolation collapses toward the barycentric mean, producing a blurred and unrealistic face, whereas MUSIC follows prototype transitions and maintains identity much longer. This difference is reflected both visually and quantitatively: MUSIC reaches the target region while preserving semantic coherence, while linear interpolation drifts off-manifold before contracting onto an averaged, non-realistic embedding.

From a computational standpoint, each MUSIC update requires solving a  $D$ -dimensional linear system of the form

$$((1 - \gamma)A^\top A + \gamma B^\top B + \lambda I) \Delta z = r,$$

where  $A$  and  $B$  contain only a small number of Jacobian rows associated with preserved and target prototypes. Since these matrices are extremely low rank relative to  $D$ , the computational cost is dominated by operations linear in the latent dimension. This makes MUSIC substantially lighter than diffusion models or autoregressive architectures, which require a full neural forward pass at every iteration. Moreover, the method does not require a generative decoder unless visual inspection of intermediate states is desired.

The method naturally inherits some limitations. Exact inversion is guaranteed only when the prototypes span the latent space, which may fail if the intrinsic dimension exceeds the number of prototypes or if prototypes are poorly distributed. In practice, this is mitigated by dimensionality reduction (e.g. PCA) or by using larger or adaptive prototype sets, such as Growing Neural Gas or Dynamic SOMs. Furthermore, since the SOM provides a piecewise-linear approximation to the data manifold, the resulting trajectories follow the geometry of the map rather than the true underlying curvature; nevertheless, the flows observed in complex domains such as face embeddings remain stable and interpretable.

Finally, the generality of the approach extends beyond classical SOMs. Because the method relies only on prototype geometry and squared-distance structure, any architecture producing a set of reference vectors with topological organization—Growing SOMs, hierarchical maps, SOM-VAE, neural gas, and related models—can serve as the backbone for inversion and for MUSIC trajectories. This creates a flexible bridge between competitive learning and modern latent representations, opening avenues for semantic editing, prototype-guided data augmentation, and interactive exploration of learned manifolds.

## 7 Conclusion

This work revisits Self-Organizing Maps through the lens of distance geometry and shows that their activation patterns contain sufficient information to recover the original input exactly. By interpreting the squared distances to prototypes as a structured system of affine constraints, we derived a linear inversion mechanism that is fully deterministic, geometrically grounded, and requires no probabilistic modeling. Building on this principle, we introduced MUSIC, a topology-aware update rule that generates smooth and interpretable semantic trajectories on the prototype lattice. MUSIC combines the selective manipulation of squared distances with Tikhonov regularization, producing stable flows within Voronoi regions and controlled reorientations across their boundaries.

Across experiments on synthetic mixtures, handwritten digits, and facial images, MUSIC reveals how SOM structure shapes latent dynamics. On a GMM, the method exhibits the expected behaviour of a piecewise-linear flow driven by prototype geometry. On MNIST, it produces meaningful cross-class transitions with clear intermediate states and quantifiable continuity. On Labelled Faces in the Wild, MUSIC enables attribute-specific transformations and user-defined semantic edits while preserving identity and photometric coherence. These results highlight the method’s ability to operate on complex visual manifolds, maintaining both interpretability and geometric consistency.

A key strength of the framework is its architectural generality. Because inversion and MUSIC rely solely on prototype coordinates and squared-distance geometry, they extend naturally to the whole family of prototype-based models:

classical SOMs, Growing Neural Gas, Dynamic and Hierarchical SOMs, adaptive-topology variants, and hybrid approaches such as SOM-VAE. In all cases, the prototypes provide the coordinate chart while MUSIC supplies the continuous dynamics.

The method also comes with clear limitations. Reconstruction fidelity is bounded by the expressiveness of the latent basis (e.g., PCA, autoencoder embeddings), and cannot match the realism of modern generative decoders. The SOM approximates the data manifold only piecewise linearly, so curvature is captured discretely rather than continuously. Nonetheless, these constraints are precisely what endow the approach with interpretability: prototype geometry makes latent transitions transparent, stable, and semantically meaningful.

Overall, this work bridges classical competitive learning with modern latent-space analysis. SOM inversion transforms prototype maps into deterministic coordinate charts, and MUSIC provides a mechanism for navigating them in a controlled, topology-aware fashion. This combination enables interpretable semantic exploration, latent editing, and data augmentation, and indicates a broader role for prototype-based representations within geometric and generative machine learning.

## References

- [1] Teuvo Kohonen. Self-organized formation of topologically correct feature maps. *Biological cybernetics*, 43(1):59–69, 1982.
- [2] Teuvo Kohonen. The basic som. In *Self-organizing maps*, pages 105–176. Springer, 2001.
- [3] Gert Hauske. A self organizing map approach to image quality. *Biosystems*, 40(1-2):93–102, 1997.
- [4] Anthony Filippi, Iliyana Dobreva, Andrew G. Klein, and John R. Jensen. Self-organizing map-based applications in remote sensing. In *Self-Organizing Maps*. IntechOpen, 2010.
- [5] Teuvo Kohonen. *Self-organization and associative memory*, volume 8. Springer Science & Business Media, 2012.
- [6] Janne Nikkilä, Petri Törönen, Samuel Kaski, Jarkko Venna, Eero Castrén, and Garry Wong. Analysis and visualization of gene expression data using self-organizing maps. *Neural networks*, 15(8-9):953–966, 2002.
- [7] Jukka Heikkonen and Pasi Koikkalainen. 10 - self-organization and autonomous robots. In Omid Omidvar and Patrick van der Smagt, editors, *Neural Systems for Robotics*, pages 297–337. Academic Press, Boston, 1997.
- [8] Juha Vesanto. *Data exploration process based on the self-organizing map*. Helsinki University of Technology, 2002.
- [9] Bernd Fritzke. A growing neural gas network learns topologies. *Advances in neural information processing systems*, 7, 1994.
- [10] Damminda Alahakoon, Saman K. Halgamuge, and Bala Srinivasan. Dynamic self-organizing maps with controlled growth for knowledge discovery. *IEEE Transactions on neural networks*, 11(3):601–614, 2000.
- [11] Michael Dittenbach, Dieter Merkl, and Andreas Rauber. The growing hierarchical self-organizing map. In *Proceedings of the IEEE-INNS-ENNS International Joint Conference on Neural Networks. IJCNN 2000. Neural Computing: New Challenges and Perspectives for the New Millennium*, volume 6, pages 15–19. IEEE, 2000.
- [12] Vincent Fortuin, Matthias Hüser, Francesco Locatello, Heiko Strathmann, and Gunnar Rätsch. Som-vae: Interpretable discrete representation learning on time series. *arXiv preprint arXiv:1806.02199*, 2018.
- [13] Diederik P Kingma and Max Welling. Auto-encoding variational bayes. *arXiv preprint arXiv:1312.6114*, 2013.
- [14] Aaron Van Den Oord, Oriol Vinyals, et al. Neural discrete representation learning. *Advances in neural information processing systems*, 30, 2017.
- [15] Jonathan Ho, Ajay Jain, and Pieter Abbeel. Denoising diffusion probabilistic models. *Advances in neural information processing systems*, 33:6840–6851, 2020.
- [16] Leonard M. Blumenthal. *Theory and Applications of Distance Geometry*. Oxford University Press, 1953.
- [17] John Clifford Gower. Properties of euclidean and non-euclidean distance matrices. *Linear algebra and its applications*, 67:81–97, 1985.
- [18] Leo Liberti, Carlile Lavor, Nelson Maculan, and Antonio Mucherino. Euclidean distance geometry and applications. *SIAM review*, 56(1):3–69, 2014.
- [19] Thomas H Meyer and Ahmed F Elaksher. Solving the multilateration problem without iteration. *Geomatics*, 1(3):324–334, 2021.
- [20] Leonard Asimow and Ben Roth. The rigidity of graphs. *Transactions of the American Mathematical Society*, 245:279–289, 1978.
- [21] Teuvo Kohonen. The self-organizing map. *Proceedings of the IEEE*, 78(9):1464–1480, 1990.
- [22] Marie Cottrell, Jean-Claude Fort, and Gilles Pagès. Theoretical aspects of the som algorithm. *Neurocomputing*, 21(1-3):119–138, 1998.
- [23] Juha Vesanto. Som-based data visualization methods. *Intelligent data analysis*, 3(2):111–126, 1999.
- [24] Christopher M. Bishop, Markus Svensén, and Christopher K.I. Williams. Gtm: The generative topographic mapping. *Neural computation*, 10(1):215–234, 1998.
- [25] Joshua B. Tenenbaum, Vin de Silva, and John C. Langford. A global geometric framework for nonlinear dimensionality reduction. *science*, 290(5500):2319–2323, 2000.
- [26] Michael M. Bronstein, Joan Bruna, Yann LeCun, Arthur Szlam, and Pierre Vandergheynst. Geometric deep learning: Going beyond euclidean data. *IEEE Signal Processing Magazine*, 2017.
- [27] Helge Ritter, Thomas Martinetz, and Klaus Schulten. *Neural Computation and Self-Organizing Maps; An Introduction*. Addison-Wesley Longman Publishing Co., Inc., 1992.

- [28] Hujun Yin and Nigel M Allinson. Self-organizing mixture networks for probability density estimation. *IEEE Transactions on Neural Networks*, 12(2):405–411, 2001.
- [29] Yoshua Bengio, Aaron Courville, and Pascal Vincent. Representation learning: A review and new perspectives. *IEEE transactions on pattern analysis and machine intelligence*, 35(8):1798–1828, 2013.
- [30] Kimmo Kiviluoto. Topology preservation in self-organizing maps. In *Proceedings of International Conference on Neural Networks (ICNN'96)*, volume 1, pages 294–299. IEEE, 1996.
- [31] Ralph A Willoughby. Solutions of ill-posed problems (a.n. tikhonov and v.y. arsenin). *Siam Review*, 21(2):266, 1979.
- [32] Ralph A. Willoughby. Solutions of ill-posed problems (a. n. tikhonov and v. y. arsenin). *SIAM Review*, 21(2):266–267, 1979.
- [33] Heinz Werner Engl, Martin Hanke, and Andreas Neubauer. Regularization of inverse problems,(1996). *Mathematics and its Applications*, 2000.
- [34] Per Christian Hansen. *Rank-deficient and discrete ill-posed problems: numerical aspects of linear inversion*. SIAM, 1998.
- [35] Pierre-Antoine Absil, Robert Mahony, and Rodolphe Sepulchre. *Optimization algorithms on matrix manifolds*. Princeton University Press, 2008.
- [36] Shun-ichi Amari. *Information geometry and its applications*, volume 194. Springer, 2016.
- [37] Hujun Yin. The self-organizing maps: background, theories, extensions and applications. In *Computational intelligence: A compendium*, pages 715–762. Springer, 2008.
- [38] Gary B Huang, Marwan Mattar, Tamara Berg, and Eric Learned-Miller. Labeled faces in the wild: A database forstudying face recognition in unconstrained environments. In *Workshop on faces in'Real-Life'Images: detection, alignment, and recognition*, 2008.
- [39] Matthew Turk and Alex Pentland. Eigenfaces for recognition. *Journal of cognitive neuroscience*, 3(1):71–86, 1991.
- [40] Yann LeCun, Léon Bottou, Yoshua Bengio, and Patrick Haffner. Gradient-based learning applied to document recognition. *Proceedings of the IEEE*, 86(11):2278–2324, 1998.

## Supplementary Material

### S1 Radial-tangential decomposition and global isodistance preservation

Consider a fixed input  $z \in \mathbb{R}^D$  and a set of SOM prototypes  $\{w_j\}_{j=1}^N$ . The squared-distance activation of prototype  $j$  is

$$a_j(z) = \|z - w_j\|^2,$$

with first-order change under a small perturbation  $\Delta z$  given by

$$\Delta a_j \approx 2(z - w_j)^\top \Delta z.$$

Thus, preserving the distance to prototype  $j$  to first order amounts to enforcing

$$(z - w_j)^\top \Delta z = 0,$$

i.e.,  $\Delta z$  lies in the orthogonal complement of the radial direction  $z - w_j$ .

Fix a reference prototype  $w_k$  and define  $x = z - w_k$ . We decompose any perturbation as

$$\Delta z = \Delta z_{\parallel} + \Delta z_{\perp}, \quad \Delta z_{\parallel} = \alpha x, \quad x^\top \Delta z_{\perp} = 0.$$

By construction, the parallel component  $\Delta z_{\parallel}$  controls the first-order change of the distance to  $w_k$ , while the orthogonal component  $\Delta z_{\perp}$  lies in the tangent subspace of the local isodistance manifold around  $z$  relative to  $w_k$ .

To see why  $\Delta z_{\perp}$  also preserves the distances to *all* prototypes to first order, note that

$$z - w_j = (z - w_k) + (w_k - w_j) = x + c_j,$$

where  $c_j = w_k - w_j$  is a constant vector independent of  $\Delta z$ . Hence the family of radial directions  $\{z - w_j\}_{j=1}^N$  lies in an affine translate of the one-dimensional subspace spanned by  $x$ :

$$z - w_j \in x + \text{span}\{c_j : j = 1, \dots, N\}.$$

As a consequence, all first-order distance changes can be written as

$$\Delta a_j \approx 2(z - w_j)^\top \Delta z = 2(x + c_j)^\top \Delta z = 2x^\top \Delta z + 2c_j^\top \Delta z.$$

If we choose  $\Delta z_{\perp}$  such that  $x^\top \Delta z_{\perp} = 0$ , then

$$\Delta a_j^{(\perp)} \approx 2(z - w_j)^\top \Delta z_{\perp} = 2x^\top \Delta z_{\perp} + 2c_j^\top \Delta z_{\perp} = 2c_j^\top \Delta z_{\perp}.$$

The vectors  $c_j = w_k - w_j$  are fixed prototype offsets that do not depend on the current point  $z$ . Although their magnitudes may vary across prototypes, the corresponding contributions  $c_j^\top \Delta z$  remain uniformly bounded. In contrast, the shared term

$$x = z - w_k$$

captures the large-scale geometry of  $z$  relative to the SOM prototypes, and the component  $x^\top \Delta z$  typically dominates the first-order variation of all squared distances. Thus, a perturbation  $\Delta z$  decomposes into a dominant component along  $x$ , which controls the primary variation of  $\|z - w_j\|^2$ , and a residual component orthogonal to  $x$ , whose effect is mediated only through the bounded offsets  $c_j$ . Consequently, the contribution of  $\Delta z_{\perp}$  to the squared distances is much smaller—effectively a second-order effect—compared to the variation produced by the component of  $\Delta z$  parallel to  $x$ .

Figure 3 illustrates this decomposition in  $\mathbb{R}^2$ : the radial direction  $x = z - w_k$  controls distance changes to the reference prototype, while tangential directions orthogonal to  $x$  induce negligible first-order changes in the distances to all prototypes.

**Typical dependence on the ambient dimension  $D$ .** The preceding argument shows that tangential motion eliminates the shared contribution  $x^\top \Delta z$  and leaves only the residual terms  $c_j^\top \Delta z_{\perp}$ . To make the dependence on  $D$  explicit, we analyze the typical magnitude of these residual dot products when  $\Delta z_{\perp}$  is chosen without preferential alignment inside the  $(D-1)$ -dimensional subspace orthogonal to  $x$ .

Let  $\mathcal{T} := \{u \in \mathbb{R}^D : x^\top u = 0, \|u\| = 1\}$  be the unit sphere in the tangential subspace, and write  $\Delta z_{\perp} = \eta u$  with  $u \in \mathcal{T}$  and step length  $\eta > 0$ . Since  $u \perp x$ , only the component of  $c_j$  orthogonal to  $x$  contributes:

$$c_{j,\perp} := \left( I - \frac{xx^\top}{\|x\|^2} \right) c_j, \quad c_j^\top u = c_{j,\perp}^\top u.$$

Assume that  $u$  is uniformly distributed on  $\mathcal{T}$  (i.e., an isotropic direction in the tangential subspace). By rotational invariance in the  $(D-1)$ -dimensional subspace, for any fixed vector  $v$  with  $v \perp x$  and  $\|v\| = 1$ , the random variable  $v^\top u$  has the same distribution as the first coordinate of a uniform point on  $\mathbb{S}^{D-2}$ . In particular, it is mean-zero, with variance

$$\mathbb{E}[(v^\top u)^2] = \frac{1}{D-1}. \quad (8)$$

Therefore, for each prototype  $j$ ,

$$\mathbb{E}[(c_j^\top u)^2] = \mathbb{E}[(c_{j,\perp}^\top u)^2] = \frac{\|c_{j,\perp}\|^2}{D-1}, \quad \Rightarrow \quad |c_j^\top \Delta z_\perp| \text{ is typically of order } \eta \frac{\|c_{j,\perp}\|}{\sqrt{D-1}}. \quad (9)$$

Recalling  $\Delta a_j^{(\perp)} \approx 2c_j^\top \Delta z_\perp$ , this yields the typical scaling

$$|\Delta a_j^{(\perp)}| \approx 2|c_j^\top \Delta z_\perp| \sim 2\eta \frac{\|c_{j,\perp}\|}{\sqrt{D-1}},$$

showing that tangential perturbations become increasingly close to isometries as  $D$  grows (in a typical-case sense).

A high-probability bound follows from standard concentration on the sphere. For  $u$  uniform on  $\mathcal{T}$  and any fixed  $v \perp x$  with  $\|v\| = 1$ ,

$$\mathbb{P}(|v^\top u| \geq t) \leq 2 \exp\left(-\frac{(D-2)t^2}{2}\right). \quad (10)$$

Applying (10) to  $v = c_{j,\perp}/\|c_{j,\perp}\|$  and a union bound over  $j = 1, \dots, N$  gives that, with probability at least  $1 - \delta$ ,

$$\max_{1 \leq j \leq N} |c_j^\top u| = \max_{1 \leq j \leq N} |c_{j,\perp}^\top u| \leq \|c_\perp\|_{\max} \sqrt{\frac{2 \log(2N/\delta)}{D-2}}, \quad \|c_\perp\|_{\max} := \max_j \|c_{j,\perp}\|. \quad (11)$$

Hence,

$$\max_{1 \leq j \leq N} |\Delta a_j^{(\perp)}| \approx 2\eta \max_j |c_j^\top u| \lesssim 2\eta \|c_\perp\|_{\max} \sqrt{\frac{2 \log(2N/\delta)}{D-2}}. \quad (12)$$

This bound makes explicit that, as long as  $D \gg \log N$ , tangential steps are simultaneously near-isometric for all prototypes with high probability.

We stress that these scalings describe typical isotropic directions in the tangential subspace; they can be weakened if the latent geometry is strongly anisotropic or if the offsets  $\{c_j\}$  are systematically aligned with a low-dimensional set of semantic directions.

## S2 Tikhonov-regularized quadratic energy

The Manifold-Aware Unified SOM Inversion and Control (MUSIC) framework defines at each iteration a perturbation  $\Delta z \in \mathbb{R}^D$  of an input vector  $z$  that modulates the squared distances to the prototypes  $\{w_j\}_{j=1}^N$  of a Self-Organizing Map (SOM).

The activation of prototype  $j$  is  $a_j(z) = \|z - w_j\|^2$  with Jacobian  $J_j(z) = \nabla_z a_j(z) = 2(z - w_j)^\top$ . For small displacements  $\Delta z$ , the first-order expansion  $a_j(z + \Delta z) \approx a_j(z) + J_j(z)\Delta z$  describes the local change in activation space.

Given a subset  $S$  of prototypes whose activations should remain approximately constant (preservation set) and a subset  $T$  whose activations should change toward prescribed values (target set), one defines row-normalized Jacobians  $A_S \in \mathbb{R}^{|S| \times D}$  and  $B_T \in \mathbb{R}^{|T| \times D}$ , together with a target activation increment  $b \in \mathbb{R}^{|T|}$ .

The preservation constraint is  $A_S \Delta z \approx 0$ , while the attraction constraint is  $B_T \Delta z \approx b$ . Because these constraints may be redundant or inconsistent, MUSIC formulates the update as the minimizer of a Tikhonov-regularized quadratic energy

$$E_\gamma(\Delta z) = (1 - \gamma)\|A_S \Delta z\|^2 + \gamma\|B_T \Delta z - b\|^2 + \lambda\|\Delta z\|^2, \quad \gamma \in [0, 1], \quad \lambda > 0.$$

The first two terms correspond to preservation and attraction, balanced by the parameter  $\gamma$ , while the last term introduces a Tikhonov regularizer that stabilizes the inverse problem and controls the magnitude of the perturbation. The presence of  $\lambda > 0$  ensures that the energy is strongly convex even when the Jacobians are rank-deficient, thus guaranteeing a unique and stable solution.

Let  $H = (1 - \gamma)A_S^\top A_S + \gamma B_T^\top B_T + \lambda I_D$  and  $r = \gamma B_T^\top b$ . The minimizer  $\Delta z^*$  satisfies  $\nabla E_\gamma(\Delta z) = 2(H\Delta z - r) = 0$  and is therefore

$$\Delta z^* = H^{-1}r = \left( (1 - \gamma)A_S^\top A_S + \gamma B_T^\top B_T + \lambda I \right)^{-1} \gamma B_T^\top b.$$

Since  $H - \lambda I$  is positive semidefinite, and  $\lambda I$  is positive definite ( $H \succeq \lambda I \succ 0$ ), the solution exists, is unique, and depends smoothly on the data.

### S3 Tikhonov regularization

The term ‘‘Tikhonov regularization’’ refers to the fact that  $\lambda\|\Delta z\|^2$  not only penalizes the Euclidean norm of  $\Delta z$  but regularizes the inversion of the composite linear operator that maps input perturbations to activation changes. Without it, the least-squares system could be ill-posed: small perturbations in the data or in the Jacobians would produce large, unstable changes in  $\Delta z$ . The regularizer acts as a spectral filter on the singular values of the operator.

If we stack the preservation and attraction terms into a single least-squares system,

$$E(\Delta z) = \|M\Delta z - y\|^2 + \lambda\|\Delta z\|^2, \quad M = \begin{bmatrix} \sqrt{1-\gamma} A_S \\ \sqrt{\gamma} B_T \end{bmatrix}, \quad y = \begin{bmatrix} 0 \\ \sqrt{\gamma} b \end{bmatrix},$$

the normal equations read  $(M^\top M + \lambda I)\Delta z = M^\top y$ , yielding the closed-form solution

$$\Delta z^* = (M^\top M + \lambda I)^{-1} M^\top y.$$

Let  $M = U\Sigma V^\top$  be the singular-value decomposition (SVD) of  $M$ , with orthogonal matrices  $U \in \mathbb{R}^{p \times p}$ ,  $V \in \mathbb{R}^{D \times D}$ , and diagonal  $\Sigma = \text{diag}(\sigma_1, \dots, \sigma_r)$  containing the non-negative singular values  $\sigma_k$  of  $M$ . Then  $M^\top M = V\Sigma^\top\Sigma V^\top = V \text{diag}(\sigma_k^2) V^\top$ , and substituting this expression into the normal equations gives

$$(V(\Sigma^\top\Sigma + \lambda I)V^\top)\Delta z = V\Sigma^\top U^\top y.$$

Multiplying on the left by  $V^\top$  (since  $V$  is orthogonal) and defining  $\tilde{z} = V^\top\Delta z$  decouples the system into scalar equations  $(\sigma_k^2 + \lambda)\tilde{z}_k = \sigma_k(u_k^\top y)$ . Solving for each component yields

$$\tilde{z}_k = \frac{\sigma_k}{\sigma_k^2 + \lambda} \langle y, u_k \rangle, \quad \Delta z^* = V\tilde{z} = \sum_k \frac{\sigma_k}{\sigma_k^2 + \lambda} \langle y, u_k \rangle v_k.$$

Each triplet  $(u_k, v_k, \sigma_k)$  corresponds to a singular mode of the linear operator  $M$ : the vector  $v_k$  is a direction in input space,  $u_k$  its corresponding direction in activation space, and  $\sigma_k$  measures the sensitivity of activations to perturbations along  $v_k$ . The factor  $\sigma_k/(\sigma_k^2 + \lambda)$  is the *Tikhonov filter factor*, which controls how much each mode contributes to the final update. For well-conditioned directions with  $\sigma_k^2 \gg \lambda$ , this factor approaches  $1/\sigma_k$ , so those modes are effectively inverted. For ill-conditioned directions with  $\sigma_k^2 \ll \lambda$ , the factor shrinks to  $\sigma_k/\lambda$ , strongly suppressing unstable components. Hence the Tikhonov regularizer acts as a *spectral low-pass filter* on the Jacobian operator  $M$ : it preserves well-supported modes and damps those that correspond to redundant or noisy directions in the activation geometry. Geometrically, the regularizer enforces smoothness by limiting the amplitude of  $\Delta z$  in directions where the mapping from input to activation is uncertain or degenerate. This explains why the Tikhonov formulation yields numerically stable and geometrically smooth perturbations, in contrast to the unregularized least-squares inverse that would amplify small singular values and produce erratic updates. In the context of MUSIC, this spectral filtering plays a crucial role: since the Jacobians of SOM activations are often highly correlated, some input directions change many activations in a similar way, producing nearly singular modes. The Tikhonov filter suppresses these ill-conditioned modes, ensuring that the resulting perturbation  $\Delta z^*$  follows a coherent and stable trajectory in the latent space. In summary, the decomposition

$$\Delta z^* = \sum_k \frac{\sigma_k}{\sigma_k^2 + \lambda} \langle y, u_k \rangle v_k$$

shows that Tikhonov regularization is not merely an  $L_2$  penalty but an explicit spectral smoothing mechanism that stabilizes the inversion of the activation Jacobian and governs the smoothness of the induced dynamics in MUSIC.

The multiplicative factor  $\sigma_k/(\sigma_k^2 + \lambda)$  attenuates components associated with small singular values, suppressing noisy or high-frequency directions in the null space of  $M$ . This mechanism is the hallmark of Tikhonov regularization and explains why it produces smoother, numerically stable perturbations compared to an unregularized least-squares inverse. The operator  $H$  inherits strong convexity from the  $\lambda I$  term, which bounds its condition number  $\kappa(H) \leq \|H\|/\lambda$ . As a consequence, the solution satisfies  $\|\Delta z^*\| \leq \lambda^{-1}\|r\|$ , and its sensitivity to data perturbations is bounded by  $\|\delta\Delta z\| \leq \lambda^{-1}\|\delta r\| + O(\kappa(H)\|\delta H\|)$ . The parameter  $\lambda$  therefore tunes the bias-variance tradeoff: increasing it improves numerical stability at the cost of smaller update amplitudes, while decreasing it recovers the least-squares solution but may amplify noise.

## S4 Probabilistic interpretation

From a probabilistic viewpoint, the quadratic energy  $E_\gamma$  can be interpreted as the negative log-posterior of a Gaussian Bayesian model that links input perturbations  $\Delta z$  to desired activation changes  $b$ . The relation between the two is modeled as a noisy linear observation process

$$B_T \Delta z = b + \varepsilon, \quad \varepsilon \sim \mathcal{N}(0, \sigma^2 I),$$

where  $\varepsilon$  represents random uncertainty or measurement noise in the target activation constraints. This defines the likelihood

$$p(b | \Delta z) \propto \exp\left[-\frac{1}{2\sigma^2} \|B_T \Delta z - b\|^2\right].$$

To regularize this inverse problem, we introduce a Gaussian prior on the perturbation itself,

$$p(\Delta z) \propto \exp\left[-\frac{1}{2\tau^2} \|\Delta z\|^2\right],$$

which encodes the assumption that, a priori, large deviations in input space are unlikely and that updates should remain close to the origin (or to the current  $z$ ). The posterior over  $\Delta z$  given the observed activation change  $b$  is then

$$p(\Delta z | b) \propto p(b | \Delta z) p(\Delta z) \propto \exp\left[-\frac{1}{2} \left(\frac{1}{\sigma^2} \|B_T \Delta z - b\|^2 + \frac{1}{\tau^2} \|\Delta z\|^2\right)\right].$$

Maximizing this posterior (MAP estimation) is equivalent to minimizing its negative log, yielding

$$\Delta z^* = \arg \min_{\Delta z} \left( \frac{1}{\sigma^2} \|B_T \Delta z - b\|^2 + \frac{1}{\tau^2} \|\Delta z\|^2 \right),$$

which is precisely the Tikhonov-regularized least-squares problem with  $\lambda = \sigma^2/\tau^2$ . In this probabilistic reading, the regularization parameter  $\lambda$  is no longer arbitrary but acquires a clear meaning as the ratio between the noise variance in the measurement model and the prior variance of admissible perturbations. Large  $\lambda$  corresponds to strong confidence in the prior (small  $\tau^2$ ), producing conservative, small-amplitude updates; small  $\lambda$  corresponds to a permissive prior or highly reliable observations, allowing larger, more reactive updates.

The same reasoning extends naturally to the full MUSIC formulation, where both preservation and attraction terms appear as Gaussian likelihood components with distinct noise levels. If we denote  $\varepsilon_S \sim \mathcal{N}(0, \sigma_S^2 I)$  and  $\varepsilon_T \sim \mathcal{N}(0, \sigma_T^2 I)$  as independent noise sources for the two constraint sets, the joint likelihood reads

$$p(y | \Delta z) \propto \exp\left[-\frac{1}{2} \left(\frac{1}{\sigma_S^2} \|A_S \Delta z\|^2 + \frac{1}{\sigma_T^2} \|B_T \Delta z - b\|^2\right)\right].$$

By identifying  $\gamma = \frac{\sigma_S^{-2}}{\sigma_S^{-2} + \sigma_T^{-2}}$  and  $\lambda = (\sigma^2/\tau^2)$  with appropriate scaling, one recovers the composite quadratic energy  $E_\gamma(\Delta z)$  of Eq. (1). This shows that MUSIC can be understood as a *Bayesian inverse problem* in which the tradeoff between preservation and attraction is governed by the relative noise levels of the two constraint channels, while the Tikhonov term plays the role of a Gaussian prior on smoothness and amplitude of  $\Delta z$ .

This interpretation places MUSIC within the broader family of probabilistic inference frameworks that include ridge regression, Kalman filtering, and variational inference in Gaussian latent-variable models. In each of these, the solution represents a balance between data fidelity (likelihood) and regularity (prior), leading to minimum-variance linear estimators under Gaussian assumptions. Here, the same principle governs the flow of information between activation space and input space: the Tikhonov term ensures that the inverse mapping from activation changes to input perturbations is statistically well-posed, with  $\lambda$  acting as an interpretable signal-to-noise control parameter. Consequently, MUSIC admits a principled probabilistic foundation that connects geometric regularization with Bayesian inference, providing an additional theoretical justification for its stability and smoothness properties.

## S5 Role of the row normalization

Row normalization of  $A_S$  and  $B_T$  is crucial to make  $\gamma$  an interpretable balance parameter: without normalization, differences in the scales of the Jacobian rows would bias the optimization toward either preservation or attraction independently of  $\gamma$ . Normalization equalizes the energy contribution of each prototype, ensuring that  $\gamma$  consistently weights the two objectives. The explicit form of  $\Delta z^*$  also reveals the close connection with the so-called Tikhonov projector used for partial preservation. When only the preservation constraint is considered, minimizing  $\|A_S \Delta z\|^2 + \mu \|\Delta z\|^2$  yields the linear operator  $P_\mu = I - A_S^\top (A_S A_S^\top + \mu I)^{-1} A_S$ , which projects any direction onto the approximate null space of  $A_S$ , smoothly suppressing components that would change the preserved activations. The MUSIC update generalizes this idea by combining the projector-like preservation with the attraction term, both modulated by  $\gamma$ , under a single regularized inverse. In the limit  $\lambda \rightarrow 0$ , if the combined Jacobian  $(1 - \gamma) A_S^\top A_S + \gamma B_T^\top B_T$  is full rank, the update

converges to the exact least-squares solution; if it is rank-deficient, the Tikhonov regularizer selects the minimum-norm solution within the set of least-squares minimizers. For  $\lambda \rightarrow \infty$ , the update tends to zero, corresponding to complete damping. The limiting cases  $\gamma = 0$  and  $\gamma = 1$  represent pure preservation and pure attraction, respectively. Each MUSIC step can thus be interpreted as a regularized inverse mapping that converts infinitesimal activation changes into a stable and minimal-energy input displacement.

## S6 Free-evolution trajectories under manifold-aware and unconstrained updates

To further analyze the qualitative behaviour of MUSIC, we design a free-evolution task where the system is not given any objective other than repeatedly applying random local perturbations in activation space.

Starting from the latent representation  $z^{(0)}$  of an input face, at each step  $t$  we randomly select a prototype  $w_{j_t}$  and sample a random perturbation of its squared distance. In the **MUSIC** condition, this perturbation defines a linearized target constraint  $B_T \Delta z \approx \delta$ , while a small preservation set  $S$  (four nearest prototypes) constrains the update to remain consistent with the local SOM geometry. We compute the MUSIC direction  $d_{\text{MUSIC}}$  from the Tikhonov system  $(M^\top M + \lambda I) \Delta z = M^\top y$  and apply a normalized step  $\Delta z^{(t)} = \eta d_{\text{MUSIC}} / \|d_{\text{MUSIC}}\|$ .

In the **no-constraints** baseline, the update direction is simply the radial vector  $(z^{(t)} - w_{j_t}) / \|z^{(t)} - w_{j_t}\|$ , again rescaled to the same step length  $\eta$ . Thus, the two trajectories differ only in their *direction*, not in their magnitude.

Despite identical step sizes, the two evolutions diverge sharply: unconstrained updates rapidly push the latent representation into regions that no longer decode into realistic faces, producing severe geometric distortions. Conversely, MUSIC maintains consistency with the local SOM geometry and evolves the face smoothly along semantically meaningful variations. Figure 10 displays a typical outcome.